An immunoPET probe to SARS-CoV-2 reveals early infection of the male genital tract in rhesus macaques

Patrick J. Madden[1], Yanique Thomas[1], Robert V. Blair[2], Sadia Samer[1], Mark Doyle[2], Cecily C. Midkiff[2], Lara A. Doyle-Meyers[2], Mark E. Becker[1], Muhammad S. Arif[1], Michael D. McRaven[1], Lacy M. Simons[3, 4], Ann M. Carias[1], Elena Martinelli[1], Ramon Lorenzo-Redondo[3, 4], Judd F Hultquist[3, 4], Francois J. Villinger[5], Ronald S. Veazey[2], and Thomas J. Hope[1*]

[1]Department of Cell and Developmental Biology, Feinberg School of Medicine, Northwestern University, Chicago, Illinois, USA.

[2]Tulane National Primate Research Center, Covington, Louisiana, USA.

[3]Department of Medicine, Division of Infectious Diseases, Northwestern University Feinberg School of Medicine, Chicago, IL, USA.

[4]Center for Pathogen Genomics and Microbial Evolution, Havey Institute for Global Health, Feinberg School of Medicine, Northwestern University, Chicago, IL, USA.

[5]New Iberia Research Center, University of Louisiana-Lafayette, New Iberia, Louisiana, USA.

PET/CT detected SARS-CoV-2 infection of 4 different tissues in the male genital tract illuminates the cause of COVID-19 clinical sequalae of male sexual health and fertility

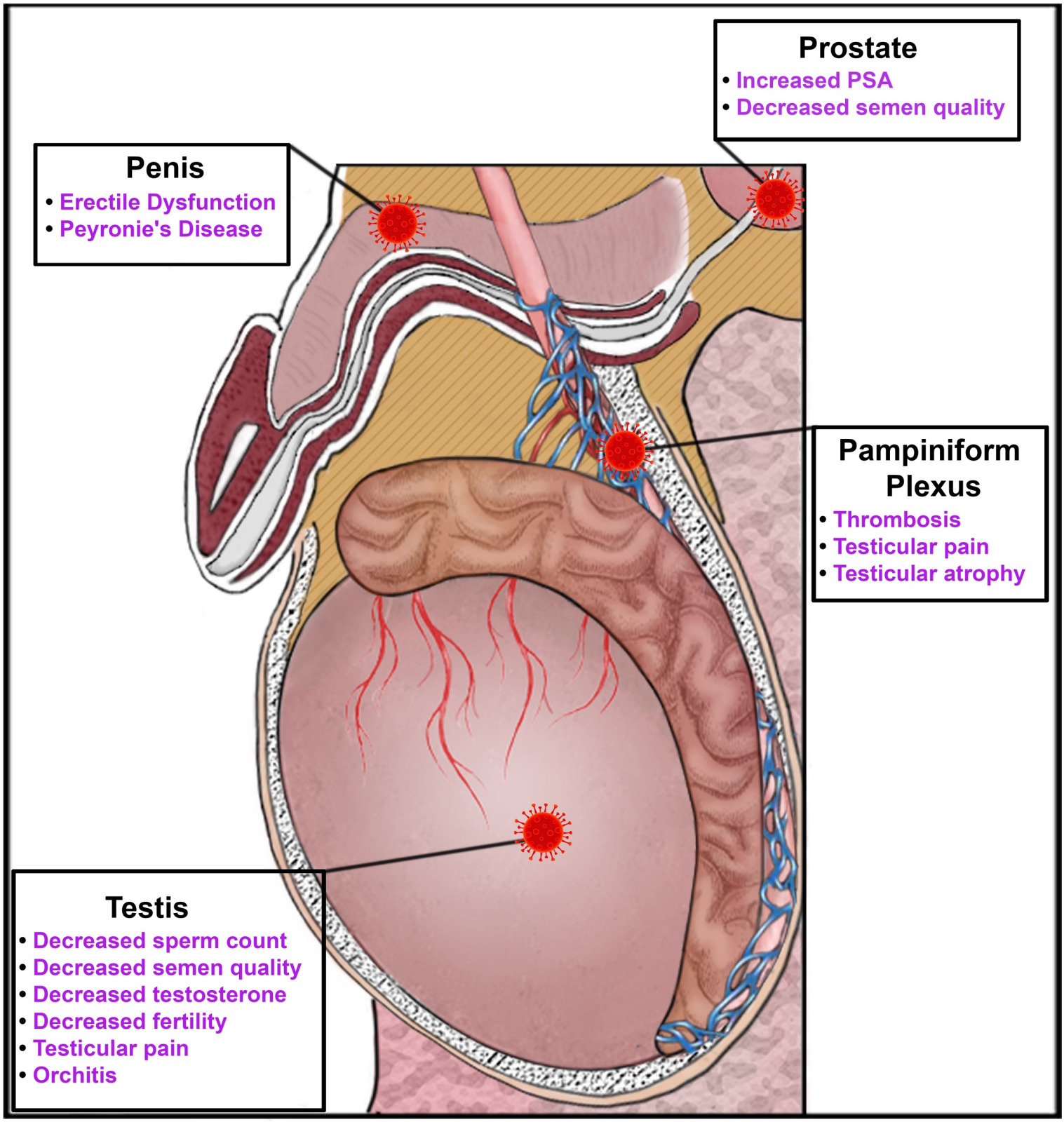

Graphic Abstract

17 **Graphic Abstract Legend: Diagram shows schematic illustration of the male genital tract of**

18 **the rhesus macaque. Virus icon shows sites of SARS-CoV-2 PET signal. Text highlighting the**

19 **clinical sequalae associated with each sight of infection is shown in text adjacent to each**

20 **infection site.**

21

22 **Abstract**

23 The systemic nature of SARS-CoV-2 infection is highly recognized, but poorly characterized. A
24 non-invasive and unbiased method is needed to clarify whole body spatiotemporal dynamics of
25 SARS-CoV-2 infection after transmission. We recently developed a probe based on the anti-
26 SARS-CoV-2 spike antibody CR3022 to study SARS-CoV-2 pathogenesis *in vivo*. Herein, we
27 describe its use in immunoPET to investigate SARS-CoV-2 infection of three rhesus macaques.
28 Using PET/CT imaging of macaques at different times post-SARS-CoV-2 inoculation, we track the
29 ^{64}Cu-labelled CR3022-F(ab')2 probe targeting the spike protein of SARS-CoV-2 to study the
30 dynamics of infection within the respiratory tract and uncover novel sites of infection. Using
31 this method, we uncovered differences in lung pathology between infection with the WA1
32 isolate and the delta variant, which were readily corroborated through computed tomography
33 scans. The ^{64}Cu-CR3022-probe also demonstrated dynamic changes occurring between 1- and
34 2-weeks post-infection. Remarkably, a robust signal was seen in the male genital tract (MGT) of
35 all three animals studied. Infection of the MGT was validated by immunofluorescence imaging
36 of infected cells in the testicular and penile tissue and severe pathology was observed in the
37 testes of one animal at 2-weeks post-infection. The results presented here underscore the
38 utility of using immunoPET to study the dynamics of SARS-CoV-2 infection to understand its
39 pathogenicity and discover new anatomical sites of viral replication. We provide direct evidence
40 for SARS-CoV-2 infection of the MGT in rhesus macaques revealing the possible pathologic
41 outcomes of viral replication at these sites.

42 **Introduction**

43 The COVID-19 pandemic has exposed the broad systemic impact that can be caused by
44 infection with a respiratory virus. Disease associated with SARS-CoV-2 infection starts with
45 respiratory pathologies and subsequently can extend to other organ systems. There is now
46 ample evidence that SARS-CoV-2 can disseminate and replicate in tissues beyond the
47 respiratory tract. A clear example is infection in the gastrointestinal (GI) tract[1]. GI symptoms,
48 including diarrhea, have been reported by individuals with mild COVID-19, and hospitalized
49 patients have exhibited more severe symptoms such as ischemia and GI bleeds [2, 3,4]. In addition,
50 it is now well established that virus is shed through the GI tract in most infected individuals and
51 wastewater screening has become an important tool for disease surveillance[5, 6]. Although less
52 studied, many other tissues have been found to harbor SARS-CoV-2. Multiple groups have
53 shown the presence of viral RNA in cardiac, renal, and brain tissues[7-10]. There is also some
54 evidence of virus in the male genital tract (MGT) [11, 12]. Furthermore, symptoms associated with
55 all these organ systems have been regularly reported[13]. Likewise, other RNA viruses have
56 documented early dissemination to distal tissues that manifest infection-related pathology over
57 the long term, including (but not limited to) polio, mumps, Ebola virus, Zika virus, and SARS-
58 CoV-1[14, 15]. For example, studies of autopsy tissue from fatalities of SARS-CoV-1 suggested that
59 it causes inflammation of the testes (orchitis)[15].

60 However, it is not yet clear if the diverse pathologies associated with SARS-CoV-2
61 infection are due to secondary effects of systemic inflammation or direct infection of tissues at
62 these distal sites. Human studies have relied on biopsies and autopsy samples to investigate
63 viral replication in sites other than the respiratory tract. The biopsy/autopsy samples only offer

64 a snapshot of the *in vivo* dynamics of disease, and there are ethical and technical difficulties in
65 obtaining them. Using animal models of infection allows for a more thorough collection and
66 investigation of affected tissues. To gain critical insights into systemic infection by SARS-CoV-2,
67 new animal models are needed to determine the extent of disseminated infection and its
68 relationship to pathogenesis.

69 SARS-CoV-2 infection in the non-human primate (NHP), rhesus macaques (*Macaca*
70 *mulatta*), recapitulates mild to moderate human disease[16-18]. Infected macaques exhibit viral
71 shedding through the respiratory tract and viral pneumonia similar to the mild form seen in
72 humans. The architecture of the respiratory tract is also generally conserved between humans
73 and macaques making them an ideal model for studying SARS-CoV-2 infection. Infection of
74 other organ systems has also been observed in macaques, most commonly in the GI tract[19, 20].
75 To gain insights into the spatiotemporal dynamics of SARS-CoV-2 during infection in the rhesus
76 macaque model, we adapted an immunoPET methodology that we are currently using to study
77 various aspects of simian immunodeficiency virus (SIV) acquisition and pathogenesis[21].
78 ImmunoPET is a molecular imaging technique that combines the specificity of an antibody-
79 based probe labeled with a radioisotope with the *in vivo* imaging power of combined positron
80 emission tomography-computed tomography (PET/CT). ImmunoPET was originally developed
81 and has been widely used in cancer research. Recently, with the advent of new antibodies and
82 better radioisotopes, immunoPET has been extended to studying many other biological
83 processes, including the *in vivo* dynamics of pathogens [22, 23]. ImmunoPET allows for repeated
84 and specific imaging of virally infected cells *in vivo* by using a radioisotope labeled antibody
85 targeting a viral protein. The non-invasive nature of PET/CT imaging allows for unbiased

86 discovery of novel tissue sites of infection through whole body imaging. Furthermore, the cell-
87 associated PET signal persists in tissue allowing for a radioactive probe-guided necropsy to help
88 determine the precise location of infected cells.

89 We have previously reported the early development of an *in vivo* antibody-based probe
90 against SARS-CoV-2 utilizing fluorescent tagging of the F(ab')2 of the anti-spike IgG CR3022[24].
91 CR3022 was one of the first monoclonal antibodies identified that bound tightly to SARS-CoV-2.
92 It was originally derived from an individual infected with SARS-CoV-1 but also exhibits tight
93 binding to the spike protein of SARS-CoV-2. Here, we extend the use of the F(ab')2 of the anti-
94 spike IgG CR3022 labelled with copper 64 (Cu^{64}) for immunoPET and targeted necropsy to study
95 systemic SARS-CoV-2 infection in the rhesus macaque model. Our results show the utility of this
96 approach in investigating SARS-CoV-2 pathogenesis in the respiratory tract and in uncovering
97 novel anatomical sites of infection. Interestingly, we detected a robust and dynamic signal in
98 the MGT including the prostate, penis, and testicles. This observation is consistent with
99 emerging and ongoing clinical observations of orchitis, oligo-/azoospermia, and erectile
100 dysfunction, and reveals these comorbidities are likely a consequence of the direct viral
101 infection of the tissues of the MGT. The successful development of an immunoPET probe to
102 study SARS-CoV-2 in the rhesus macaque challenge model will allow longitudinal studies to gain
103 insights into SARS-CoV-2 progression, dissemination, and the development of comorbidities.
104

105 **Results**

106 **Description of macaque studies and PET/CT-guided necropsy**

107 The basic process and workflow of the PET/CT guided necropsy method is shown in Fig 1A. The
108 PET/CT guided necropsy approach consists of three separate PET/CT scans that are used to map
109 probe signal at the whole animal, organ, and tissue levels. The first scan is typically ~16-24
110 hours after the injection of the radio labelled F(ab')2 probe allowing for movement into the
111 tissues[21]. This whole-body PET/CT scan (Scan 1) identifies "hot" organs and tissue areas. These
112 tissue areas are collected at necropsy immediately following the scan and subjected to a second
113 PET/CT scan (Scan 2). Tissues containing probe signal are cut into small blocks, placed in
114 cryomolds, and then rescanned (Scan 3) to identify individual "hot" tissues/blocks that likely
115 contain foci of virally infected cells. These "hot" tissues can then be used for downstream
116 characterization including RNA quantification and different types of microscopic analyses
117 characterizing virally infected cells.

118 The SARS-CoV-2 pilot infection study design with 3 male rhesus macaques is shown in
119 Fig 1B. Based on our previous studies utilizing a fluorescently tagged F(ab')2 probe, we decided
120 to perform the first PET/CT scan 1 week after challenge. In the first study, we infected a male
121 rhesus macaque (LP14) with the WA1 isolate of SARS-CoV-2 and performed a single PET/CT
122 scan followed immediately by necropsy. In the second study, two male rhesus macaques were
123 infected with the Delta variant of SARS-CoV-2, and both underwent a PET/CT scan 1 week after
124 infection. One of the animals (IN22) was scanned twice after a single probe injection and
125 necropsied after the 2nd scan. The early scan of IN22 was done 3 hours after injection of the
126 ^{64}Cu-labelled F(ab')2 probe and a second whole-body scan was done ~21 hours after probe
127 injection with the PET/CT guided necropsy done immediately after. For the third animal (JF82),
128 the 1st PET/CT scan at week 1 post infection was performed ~22 hours after IV probe

129 administration. On day 13, this same animal, JF82, was evaluated at week 2 post-infection by
130 whole-body scan 18 hours after probe administration followed by necropsy and subsequent
131 scans.
132
133 **SARS-CoV-2 infection characteristics**
134 SARS-CoV-2 infection of the 3 animals was monitored via classical hematoxylin and eosin
135 (H&E) staining for evaluation of lesions in lung tissue (Fig 1C-E) and via quantification of
136 genomic and subgenomic RNA in nasal swabs and saliva (Fig 1F, G). Pathology varied from
137 minimal in LP14 (Fig 1C), to mild in IN22 (Fig 1D) and JF82 (Fig 1E). These findings are consistent
138 with the pulmonary pathology of SARS-CoV-2 infected rhesus macaques observed in other
139 studies performed at the Tulane National Primate Research Center[17, 25]. The pulmonary
140 pathology consisted of variable interstitial inflammation and type II pneumocyte hyperplasia
141 (IN22 and JF82), which in the most severely affected animal (IN22) also exhibited prominent
142 atypia. Fig 1F and G shows the level of genomic (Fig 1F) and subgenomic (Fig 1G) RNA in nasal
143 swabs and saliva for all 3 animals. No obvious differences were noted in viral loads between the
144 3 animals.
145
146 **Distribution of SARS-CoV-2 signal after 1 week of infection with the WA1 isolate**
147 The three PET/CT scans of LP14, including the whole body (Fig 2A and B, S1-video), the organ
148 scan (Fig 2C, D, and E, S2-video) and the tissue scan (Fig 2F), revealed probe signal at a number
149 of distinct anatomical sites. As expected, there was a strong signal in the kidneys, which is a
150 consequence of the excretion of the radiolabeled probe. To better evaluate the probe signal in

151 the lungs, the 3D reconstruction of the lungs was isolated from the PET datasets, and the lung
152 signal was projected over the CT reconstruction of the skeleton (Fig 2G and H, S3-video). The
153 signal associated with the lungs was diffuse and quite uniform throughout the tissue as
154 observed in the whole animal scan. This is more evident in the projection of the lung signal
155 without CT (Fig 2I and J, S3-video). However, the lung signal was more evident in the post
156 necropsy organ scan when the intact respiratory tract including the tongue were scanned again
157 (Fig 2C). In this case, lungs were no longer inflated within the body increasing signal density,
158 leading to higher signal in the 2nd scan. Two different respiratory tract z-series images (Fig 2K
159 and L) reveal a focus of signal associated with the base of the tongue, overlapping with the
160 pharynx as evidenced by the cartilaginous structures seen in the CT. There were abundant small
161 foci of signal distributed throughout the lung tissue, often adjacent to the trachea and bronchi
162 as they branch out into the lungs. In addition, the z-series' reveal that the observed PET signal is
163 associated with the tissues and not with the open airways of the bronchus and ever narrowing
164 bronchi. Immunofluorescence microscopy revealed areas of infected cells lining alveoli in lung
165 tissue sections that had PET/CT signal (Fig 2M and N) confirming the specificity of the PET
166 signal.

167 In contrast to the weak, diffuse signal associated with the lungs, there was a strong and
168 more focal PET signal within the MGT as shown in the front (Fig 3A) and side (Fig 3B-C) views
169 (S4-video). The testes have a generally diffuse signal with some concentration of signal at the
170 dorsal and ventral surface of both LP14 testes. The MGT of the rhesus macaque is similar to
171 that of humans but is distinct in several ways. Most notably, it is primarily retracted within the
172 body covered by a prepuce with a small bone located within the glans penis known as the

173 baculum (visible in the CT scan of the animals, Fig 3B and C, red arrow). There was a very
174 pronounced PET signal associated with the root of the penile tissues, which is buried within the
175 abdomen. The 3D PET signal was projected in green in a front (Fig 3D) and side view (Fig 3E) to
176 better illustrate the signal associated with the MGT and to visualize the signal from the root of
177 the penis (see S5-video). The localization of the PET signal for the penis and testes in the
178 context of the skeletal CT signal is shown in three different projections in panels 3F, 3H, and 3J,
179 and isolated in panels 3G, 3I, and 3K (S6-video). The testis overlays shown in Fig 3L-O reveal
180 that the PET signal is primarily associated with the testis and is distributed throughout the
181 testicular tissue. There is also some potential signal associated with the epididymis.
182 In anticipation of a potential signal in the testes, which are known to express the SARS-
183 CoV-2 receptor ACE2, we had designated the testes to be a component of the organ scan post
184 necropsy. Unfortunately, much of the penis tissue was discarded at the necropsy of LP14,
185 though we were able to isolate a small piece of penile tissue remaining within the abdomen.
186 This small piece of penile tissue retained PET signal as can be seen in Fig 2 (Fig 2F: row 8 column
187 5, Fig S2). To potentially identify infected cells within the testicular tissue of LP14, we evaluated
188 tissue sections for expression of SARS-CoV-2 proteins and host proteins using
189 immunofluorescence microscopy. In LP14, we found that ACE2 is expressed in the peritubular
190 myoid and Sertoli cells surrounding/lining the base of the seminiferous tubules (Fig 4A). Next,
191 we stained testicular tissue sections from LP14 with an anti-SARS-CoV-2 guinea pig serum.
192 Infected cells were evident in seminiferous tubules but were not widely distributed and were
193 instead localized in small clusters of cells at the base of the seminiferous tubules (Fig 4B).
194 Infection of Leydig and other interstitial cells could not be evaluated due to loss of these cells

195 during tissue processing. To further investigate the phenotype of infected cells, we stained with
196 markers to help identify peritubular myoid cells (smooth muscle actin) and Sertoli cells
197 (vimentin). SARS-CoV-2 anti-serum colocalized with vimentin staining at the base of the tubules,
198 indicating that Sertoli cells are being infected (Fig 4C). However, SARS-CoV-2 staining was
199 sometimes observed in cells negative for vimentin indicating that cellular targets exist in
200 addition to Sertoli cells (presumably germ cells because of their localization) (Fig 4C, arrow
201 heads).
202
203 **Distribution of SARS-CoV-2 Delta variant signal after 1 week of infection**
204 Because of the mild disease manifestations of SARS-CoV-2 WA1 seen in many rhesus macaque
205 studies, we utilized the Delta variant for the next set of animals, which had become the
206 dominant circulating variant at the time of this study[26]. For IN22, at 1-week post infection, we
207 performed 2 PET/CT scans at 3- and 21-hours post probe injection to gain insights into the
208 dynamics of the probe distribution over time. This is an important aspect of probe function
209 because as the probe distributes from circulation into the tissue it will encounter virally
210 infected cells which will affect its distribution pattern. The three PET/CT scans of IN22, the
211 whole body (Fig 5A-D and S7-video, S8-video), the organ scan (Fig 5E-H and S9-video) and the
212 tissue scan (Fig 5I) are shown in Fig 5.
213 The front and side views of the 3-hour scan (Fig 5A, B and S7-video) and 21-hour scan
214 (Fig 5C, D and S8-video) reveal a highly dynamic system of probe distribution demonstrating
215 that the timing of the PET/CT scan after probe injection is an important consideration. The 3-
216 hour scan clearly captures a robust probe signal in the vasculature and chambers of the heart,

217 consistent with a large fraction of the probe still circulating in the blood after IV injection. A
218 strong lung signal is apparent in the 3-hour scan in contrast to the previous animal. Some signal
219 was also observed in the MGT with a very strong signal observed in the prostate in the 3-hour
220 scan. In the 21-hour scan, the lung probe signal remained much greater than observed in LP14
221 and was further distributed throughout the tissue. The prostate signal remained but decreased
222 substantially in the 21-hour scan while signal in the MGT was further amplified. For the most
223 part, an increase in signal was seen at tissue sites of probe labeling in the 21-hour scan. In
224 contrast, the vasculature signal decreased substantially, consistent with the movement of the
225 probe from blood, into tissues. However, some discrete probe labeling of certain vascular sites
226 remained, possibly indicating infection of the vasculature.

227 To better evaluate the probe signal in the lungs after Delta infection, the 3D
228 reconstruction of the IN22 lungs was isolated from the PET datasets, and the lung signal was
229 projected over the CT reconstruction of the skeleton (Fig 6A-D, S10-video). Both the 3-hour and
230 21-hour signals are significant and localized. The lung rotation series (Fig 6E and F) reveal a
231 major signal associated with the caudodorsal portion of the right lung and less signal associated
232 with the left lung. Single z images of the PET and CT signal in sagittal and transverse sections is
233 shown in Figs 6G-J to better facilitate the analysis of the relationship of CT revealed lung
234 pathology with the PET signal. This comparison reveals an overlap of the opaque lung signal and
235 greater PET signal in the right lung in contrast to the more CT transparent left lung tissue (Fig
236 6G-J). The stronger PET signal in the right lung observed in the whole-body scan is recapitulated
237 in the organ scan (Fig 6K-O). This animal had overt gross pathology associated with the dorsal
238 aspects of the right lower lung lobe as highlighted in the magnified inset (Fig 6L).

239 Histopathology of this region revealed marked pulmonary interstitial inflammation and
240 type II pneumocyte hyperplasia (Fig 1D, and 6P-S). The projection of the PET signal over the
241 photo (6N) shows a strong PET signal in multiple lung lobes and located adjacent to the focally
242 extensive areas of consolidation (red and inflamed areas). A similar strong PET signal is
243 observed in several areas of the left lung, with a major PET signal associated with the caudal
244 aspect of the upper lobe of the left lung. An overlay of the unnormalized PET over a CT
245 projection that reveals lung structure and fluid in the lung (Fig 6O) further details the
246 relationship between the areas with evidence of pneumonia and the PET signal. The PET signals
247 tend to be adjacent to opaque regions potentially caused by fluids and the regions of
248 consolidation visible in the photo.
249 Next, we evaluated paraffin blocks of the right lower lobe by H&E (Fig 6P and R) and
250 immunofluorescent staining for SARS-CoV-2 (Fig 6Q and S). In regions of pneumonia (Fig 6P),
251 the interstitium and alveolar spaces are expanded by inflammatory infiltrate. In these same
252 regions, SARS-CoV-2 infected cells are scattered throughout (Fig 6Q). Higher magnification
253 imaging of the H&E stain (Fig 6R) reveals the inflammatory infiltrate is composed predominately
254 of macrophages with lesser neutrophils (arrowheads). Alveolar septa are frequently lined by
255 type II pneumocytes (arrows). SARS-CoV-2 staining (Fig 6S) reveals infected cells within alveoli
256 (arrows) and lining alveolar septa (arrowheads).
257 To validate the accuracy of our SARS-CoV-2 staining results, 2-color
258 immunofluorescence staining for spike and nucleocapsid was used to identify SARS-CoV-2
259 infected cells in the right lung (Fig 6T). Spectral imaging confirmed that the fluorescence signal
260 associated with the double positive cells is consistent with the specific fluorophores utilized for

261 antigen visualization. Additional fluorescent staining shows focal nature of infected cells in a
262 large piece of lung tissue (Fig 6U-W). The 2-color imaging is a powerful method to validate the
263 identification of SARS-CoV-2 infected cells. Spectral imaging of left lung tissue stained for NC
264 and dsRNA was used as an alternate approach to identify infected cells (Fig is shown in panels
265 6X-Z). The spectrum shown in Fig 6Z confirms that the cells identified in panel 6Y are
266 specifically double stained with the antibodies to dsRNA and SARS-CoVCoV-2 NC.
267 To evaluate the probe signal in the MGT after Delta infection, we compared the 3-hour
268 and 21-hour PET/CT signal in the IN22 MGT (Fig 7A-D); the isolated PET signal of the MGT of
269 both scans is shown below (Fig 7E-H). A signal is apparent in the base of the testes that
270 becomes more diffuse at the 21-hour timepoint. There is also a signal apparent just above both
271 testes in the 3-hour scan that increases at 21-hours and is most prominent above the right teste
272 (Fig 7A-H, indicated by white asterisk). Examination of both scans indicates that the probe
273 signal was initially associated with the vasculature, but it persisted and accumulated adjacent to
274 the top of testes in the 21-hour scan. This PET signal is associated with the vasculature of the
275 spermatic cord as is visible in the CT projections and the PET overlays in the 21-hour scan (Fig
276 7I-L) and after the necropsy (Fig 7M-P). The post necropsy signal matches the *in vivo* scan with
277 the left testicle having a persistent signal throughout the spermatic cord and a more localized
278 signal on the top of the right teste. To confirm infection in these tissues, the tissue block with
279 the greatest PET signal (L Test 1, Fig 5I) was sectioned for genomic and microscopic analysis.
280 Bulk RNA was isolated from 2 tissue sections and qPCR analysis of the SARS-CoV-2 N gene
281 revealed the presence of viral RNA (2.03 Copies N1/ul). Immunofluorescence analysis of the
282 PCR positive tissue derived from the same block revealed the presence of sparse cells double

283 positive for spike and nucleocapsid primarily found in the interstitial space (Fig 7Q and R).
284 Staining of penile tissue from an uninfected macaque (Fig 7S) reveals robust ACE2 expression in
285 the venous spaces of the corpus cavernosum. Multiple SARS-CoV-2 infected cells in the penis
286 were revealed by double staining for nucleocapsid and dsRNA (J2) (Fig 7T-W).
287
288 **Longitudinal analysis of SARS-CoV-2 Delta variant distribution 1- and 2-weeks post-infection**
289 For the final pilot study, we performed two longitudinal PET/CT scans, at 1- and 2-weeks post
290 challenge with the Delta variant, on a single animal (JF82). The goal of this study was to
291 determine if the ^{64}Cu-F(ab')2 probe could provide novel insights into the spatiotemporal
292 dynamics of SARS-CoV-2 infection with sequential PET/CT scans. A front and side view of the
293 sequential PET/CT scans at 1-week (Fig 8A-B) and 2-weeks (Fig 8C-D) reveals dynamic changes
294 in various organ systems. For example, there is a decrease in the signal of the lungs between
295 week one and two while MGT signal increases. These changes are illustrated in the front (Fig
296 8E) and side (Fig 8F) view overlay of the 1-week (shown in red) and 2-week (shown in blue)
297 timepoints. Areas with blue signal indicate increased signal in week 2 relative to week 1 and
298 areas with red signal indicate where the week 1 scan had greater signal. Areas with white signal
299 indicate where there is high PET signal in both scans. The post necropsy organ scan (Fig 8G-J,
300 S7-video) and the tissue scan (Fig 8K) similarly show probe signal associated with both the lungs
301 and MGT.
302 To better compare the probe signal in the lungs of JF82 at the 1-week (Fig 9A-B) and 2-
303 week (Fig 9C-D) timepoints, the 3D reconstruction of the JF82 lungs was isolated from the PET
304 datasets and projected over the CT reconstruction of the skeleton (Fig 9A-D). Both the 1- and

305 2-week lung signals are apparent and localized with a level of signal comparable to the previous
306 animal (IN22) infected with the Delta variant. An evaluation of the data set revealed a PET
307 signal overlying a region of opacity in the lower lobe of the left lung as designated with the
308 asterisks in several of the panels (Fig 9A-B, 9G-L). The lung rotation series shown for week 1
309 (Fig 9E) and week 2 (Fig 9F) reveal a major signal associated with the dorsal side of the left lung
310 at both timepoints and less signal associated with the right lung in the week 1 scan. Evaluation
311 of signal from coronal sections of the week 1 PET/CT overlay (Fig 9G) and CT alone (Fig 9I)
312 reveals an overlap of the probe signal with an opaque region consistent with focal pneumonia.
313 It is notable that both the PET and CT signal associated with this spot in the left lung are gone in
314 the week 2 scan (Fig 9H and J). This is consistent with reports that the lung pathology observed
315 in the rhesus macaque model is most apparent after 1 week of infection and can wane by week
316 2[25]. To better illustrate the change between week 1 and week 2, the week 1 scan in red and the
317 week 2 scan in blue were overlaid with the week 1 CT signal (Fig 9K and L). Microscopic analysis
318 revealed pulmonary infiltrates were still present in the alveolar space at necropsy (Fig 1E).
319 However, no infected cells were detected with immunofluorescence using an anti-SARS-CoV-2
320 antibody in FFPE tissue. These findings are suggestive of a resolving infection which is
321 supported by the histopathology (Fig 1E) and viral RNA levels (Fig 1F and G).
322 We next evaluated the signal associated with the MGT of JF82 as illustrated in Fig 10,
323 which presents the front and near side view (~45˚) of the abdominal area of the week 1 (Fig 10A
324 and D), week 2 (10B and E), and overlay (10C and F). The overlay (Fig 10C and F) reveals the
325 dynamics of the probe signal in the MGT of JF82 in the first 2 weeks of SARS-CoV-2 infection.
326 The white signal in the overlay reveals that the probe signal is maintained in the prostate, the

327 vasculature at the base of the spermatic cord, and the base of the testes. To gain additional
328 insights into the MGT associated signal at the 2 time points, we isolated the MGT volumes and
329 3D projected the signal (Fig 10G-J). In the week 1 scan (Fig 10G-H), a signal associated with the
330 root of the penis is also apparent in addition to the signal associated with the vasculature at the
331 base of the spermatic cord and the base of the testes. In the week 2 scan, the signal becomes
332 more diffuse, spreading throughout the penis and testes, and extending into the spermatic
333 cord, especially into the right spermatic cord. To better visualize the signals associated with the
334 different tissues, we isolated the volumes containing the penile signal for the week 2 scan (Fig
335 10K-M). The signal distribution throughout the penis at week 2 is readily apparent and distinct
336 from the signal associated with the spermatic cord. It is notable that the probe signal associated
337 with the MGT becomes better distributed and more pronounced in the week 2 scan, consistent
338 with a spreading infection in the MGT between week 1 and week 2. In contrast, a focus of
339 infection in the right lung (Fig 9) of the same animal is observed in the week 1 scan and
340 resolved in the week 2 scan.

341 Histopathology of testicular tissue from JF82 revealed multifocal regions of degenerate
342 seminiferous tubules characterized by a complete loss of germ cells and spermatids (Fig 10N).
343 These regions also have evidence of edema as revealed by increased spaces between individual
344 seminiferous tubules. Degenerate seminiferous tubules occasionally contained macrophages
345 with phagocytosed spermatids, and the adjacent interstitium was infiltrated by low numbers of
346 lymphocytes and plasma cells. To further characterize the degenerative changes noted on H&E,
347 immunofluorescence for CD206 - a mannose receptor present on monocytes, macrophages[27],
348 and mature spermatids[28-30] - and caspase 3 - a cellular marker of apoptosis - was performed.

349 Degenerate seminiferous tubules were readily identified by the marked decrease in CD206
350 expression (due to loss of mature spermatids) and increased expression of caspase 3 compared
351 to adjacent, nondegenerate, tubules (Fig 10O, Q-S). Evidence of intra-tubule macrophages was
352 readily apparent (Fig. 10R, S). SARS-CoV-2 infected cells can be identified in the JF82 testes with
353 triple staining for NSP8, nucleocapsid, and SARS-CoV-2 anti-sera (Fig 10T and U).
354
355 **Comparison of PET signal between animals**
356 A comparison of the PET/CT scans of 3 SARS-CoV-2 infected rhesus macaques is revealing in
357 terms of the dynamics of infection and the utility of this technique to study COVID-19. In Fig
358 11A-D we present a comparative rotation series of the PET signal withing the lung volumes of
359 all scans. Although there are differences in the lung signal of each scan, the Delta variant
360 utilized for infection of IN22 (Fig 11B) and JF82 (Fig 11C-D) is associated with increased
361 pathology[26] (Fig 1C-E, Fig 5, and Fig 8) and increased PET signal (Fig 11B-D) without a clear
362 difference in viral load in nasal swab or saliva at 1 week after challenge (Fig 1F and G) compared
363 to LP14. This is consistent to similar viral loads between WA1 and the Delta variant in a recent
364 report[26].
365 The probe signal associated with the MGT was not anticipated, but apparent in all 3
366 animals. This reveals that infection of MGT is consistently seen in the rhesus macaque model of
367 SARS-CoV2 IN/IT challenge. A comparison of the isolated MGT PET signal from the four whole-
368 body PET scans of 3 SARS-CoV-2 infected rhesus macaques (Fig 11E-H) presented as a rotation
369 series further reveals the dynamics of SARS-CoV-2 after infection. The difference in MGT signal
370 between the animal infected with WA1 (LP14) and the animals infected with the Delta variant

371 (IN22 and JF82) at week 1 is much less pronounced than that seen in the lungs. In all week 1
372 MGT scans, the signal is asymmetrically distributed with diffuse signal throughout the testicles,
373 an increased signal at the base and top of the testes, and a signal associated with the root of
374 the penis (Fig 11E-G). The MGT PET signal is visibly increased in the week 2 scan relative to the
375 week one scan (Fig 11G, H) for JF82 indicating further spread of infection into the MGT at that
376 time. Another obvious difference between the week 1 whole-body PET scans is a variable signal
377 associated with the heart and liver as shown in Fig 11I-K. LP14 had a diffuse PET signal
378 throughout the liver (Fig 11I). In contrast, the IN22 PET signal (Fig 11J) was primarily localized
379 with the right side of the liver and in JF82 the PET signal (Fig 11K) was localized to the base of
380 the liver. Additionally, the extent of labeling of the heart is variable with JF82 and IN22 having a
381 greater signal than LP14 (Fig 11L).

382 To take advantage of the quantitative aspects of PET detection, we isolated the total
383 standard uptake value (SUV) of the PET signal associated with the CT defined volumes as
384 plotted in Fig 11L. The 3 animals scanned 1 week (W1) post SARS-CoV-2 challenge are
385 presented together for the whole-body (WB) scan signal and all evaluated tissues. The single
386 week 2 (W2) PET signal of JF82 is presented for comparison. The WB values for all scans are
387 clustered revealing the reproducible nature of evaluation of the PET signal. An increase in the
388 total SUV between week 1 and week 2 for the MGT and testes volumes is consistent with the
389 increase of signal suggested by visual inspection of the isolated tissues (Fig 10, Fig 11G and H).

390 Another relevant tissue with PET signal observed in all 3 animals is the prostate. Probe
391 labeling of the prostate first became apparent in the early PET scan (3 hr. after injection) of
392 IN22 where it was among the strongest, non-kidney associated signals (Fig 5A and B).

393 Therefore, we revaluated the PET/CT data sets for the 3 animals. We were able to detect a
394 signal associated with the prostate in all animals (marked by white asterisks, Fig 12A-F). An
395 inset showing a sagittal slice of the PET/CT shows the localization of the prostate within the
396 small white circle for each animal. PET signal was also isolated within the penile volume of the
397 whole-body scan for IN22 1-week post infection (Fig 12G-I) and 2-weeks post infection for JF82
398 (Fig 12J-L). LP14 is excluded from this analysis because the penile tissue was not collected. The
399 same general distribution of PET signal is seen in the organ scan of IN22 (Fig 12M) and JF82 (Fig
400 12N). The localization of the PET signal is further defined in the tissue scan of the cryomolds
401 shown with (Fig 12O and Q) and without (Fig 12P and R) PET signal for each animal. There is
402 PET signal associated with the penile tissue with a stronger signal associated with the penile
403 root of IN22 and the glans of JF82. This PET/CT guided necropsy of the MGT reveals a
404 persistent signal associated with the penile tissue of these 2 animals. All 3 animals had an
405 apparent PET signal associated with the testes at the 1-week timepoint and that signal
406 increased in the testes in the week 2 scan (Fig 12Q-T, quantified in Fig 11O). The
407 histopathologic analyses of the testes from all three animals are shown in Fig 12S-U. Testicular
408 degeneration was noted in seminiferous tubules of JF82 (Fig. 10N). Panels demonstrate normal
409 spermatogenesis or lack thereof in JF82 (Fig. 12N, O, R, S).
410 In addition, all animals had a PET signal located at the top of each testicle, where the
411 spermatic cord connects with testicle. A dissection of the rhesus macaque testicular anatomy is
412 shown in Fig 13A-C. The spermatic cord contains the vasculature supplying blood to the
413 testicles, the vas deferens which transports mature sperm produced in the testes, and the
414 cremaster muscle (Fig 13A). The position in natural context of the macaque penis, testes, and

415 spermatic cord are shown in Fig 13B. A magnified view of the vasculature of the pampiniform
416 plexus is shown in Fig 13C. As shown in the IN22 MGT PET/CT series (Fig 13D-G), there is a
417 major signal associated with the top of the testicles, especially the right testicle. A further
418 examination of this signal within the PET/CT data set demonstrates it is located just above the
419 testicle in the yellow volume (Fig 13D-G). This yellow volume is overlapping with a vasculature
420 structure consistent with the pampiniform plexus visualized by CT (Fig 10G and B). The signal
421 associated with the pampiniform plexus and spermatic cord is seen in the 1-week scan of all
422 animals in front (Fig 13H, J, and L) and rotate 45˚ view (Fig 13I, K, and M) outside of the ovals
423 indicating the tetes. The signal associated with the pampiniform plexus and spermatic cord for
424 LP14 can be seen outside of the white ovals (Fig 13L-Q).
425
426 **Principal component analysis of PET SUV signals**
427 The PET signal includes several parameters in each anatomical area, each of which provide
428 different insights into the distribution of the probe within the tissue. For example, the total SUV
429 (Fig 11L), provides insights into the overall signal in each tissue/animal. However, the total SUV
430 does not account for variability in tissue size and shape. The mean SUV provides insights into
431 the relative intensity of PET signal in each tissue (Fig 14A). This comparison of mean SUV reveals
432 the relative intensity of the signal across tissues, with the prostate having consistently high
433 signal in all animals. In contrast, the total SUV/whole body Total SUV for the different tissues
434 illustrates the percentages of the total whole-body signal in each tissue without consideration
435 of the size of each tissue relative to the other (Fig 14B). All 7 PET parameters for each tissue are
436 shown in the heatmap (Fig 14C), which reveals that different tissues have unique signal

437 characteristics. From this analysis, it is evident that the prostate signal of IN22 and JF82 have
438 the highest mean SUV and standard deviation with relatively a high median SUV being also seen
439 in the prostate of the 3rd animal LP14. For example, the prostate signal of IN22 and JF82 has the
440 highest mean SUV and standard deviation with relatively a high median SUV being also seen in
441 the prostate of the 3rd animal LP14, indicating a more clustered signal compared to the tissues
442 with the highest total SUV.

443 To facilitate the use of our PET data to gain insights into our data set we utilized
444 Principal Component Analysis (PCA) followed by hierarchical clustering to examine the data
445 from all scans of the 3 animals. To cluster tissues according to their SUV signal characteristics,
446 we applied PCA including all variables obtained from the SUV measurements (i.e., Total SUV,
447 Total SUV Whole Body ratio, Mean SUV, Median SUV, Standard Deviation SUV, Max SUV, and
448 Kurtosis) for each tissue and animal. After this analysis, we observed 4 different clusters that
449 correspond to tissues that display very distinct SUV signals. The clustering captures the prostate
450 signal described in the heat map where they are part of cluster 4 (dark blue group). Of note, the
451 major right lung signal of IN22 also clusters within this group, while the prostate signal of LP14
452 does not (Fig 14D). The evident PET signal observed in the lungs of the Delta variant animals
453 IN22 and JF82 are part of the cluster 3 (green group) (Fig 14D) revealing their similarity with its
454 small foci of high signal and increased kurtosis value (indicating data heavy tails or more
455 outliers) consistent with the signal variability. The higher kurtosis is also associated with penile
456 and testes signal of all the animals in the red and light blue clusters 1 and 2. This analysis allows
457 us to begin to appreciate the nature of the PET signal associated with the different tissues,
458 different animals, different viruses, and identify outliers.

459

460 **Discussion:**

461 The goal here was to develop a F(ab')2 based immunoPET probe to allow the visualization of
462 SARS-CoV-2 spike protein expression in the rhesus macaque infection model. This model is
463 clinically relevant as it was used to develop the highly successful vaccines now available against
464 SARS-CoV-2[31, 32]. The ability to detect anatomical sites of SARS-CoV-2 infection will facilitate
465 our understanding of COVID-19 disease severity and the mechanism of comorbidities in the
466 development of pathology. It could be especially useful in understanding long-COVID and its
467 underlying causes[33, 34]. This pilot study is a key step in the clinical development of this PET
468 probe to visualize SARS-CoV-2 replication and to facilitate treatments for COVID-19. The
469 distribution of the probe is complex, but it can reveal sites of SARS-CoV-2 infection in the rhesus
470 macaque model.

471 The utility of the probe is best demonstrated by the temporal association of the PET
472 probe with CT detected lung pathology between weeks 1 and 2 in JF82. A PET signal was clearly
473 associated with an opaque region (pneumonia) in the left lung in the week 1 scan, but both the
474 PET signal and CT detected pneumonia are not present in the week 2 scan, validating this
475 technique. The overlays, shown in Fig 9, further illustrate this transient lung pathology
476 detected by comparing the two PET/CT scans separated by one week. Supporting this
477 interpretation of the PET/CT data, the pathology report shows that the left lung of JF82 has
478 type II pneumocyte hyperplasia and inflammatory infiltrate consistent with the normal course
479 of infection observed in the rhesus macaque model. Overall, the lung pathology associated
480 with SARS-CoV-2 in our three animals was consistent with the observation of many infected

481 rhesus macaques where the lung pathology was typically mild and peaked at 1 week after IN/IT
482 challenge. This dynamic was generally observed for lung associated signal in this limited pilot
483 study. There was some consolidation and inflammation observed in animal IN22 and this
484 coincided with an adjacent PET signal in both animals infected with the Delta variant.
485 Further validation of the PET/CT probe's ability to identify areas of infection at sites
486 other than the lungs and its utility in understanding COVID-19 pathogenesis was the revelation
487 of a reproducible infection of the MGT. In all three animals, the probe was associated with the
488 prostate, penis, pampiniform plexus, and testicles. We have been able to identify SARS-CoV-2
489 infected cells in the testicles of all 3 animals. Comparing the longitudinal PET scans of JF82
490 reveals that while the lung pathology and signal wane between week 1 and 2, the signal of the
491 MGT, and more specifically in the testicles increases in week 2. Consistent with increased
492 testicular infection at week 2 indicated in the PET scan, H&E staining of the JF82 testes revealed
493 a unique pathology consisting of denuded stretches of the twisted and intertwined
494 seminiferous tubules (presenting as a tube cluster). Spermatids were absent in these
495 degenerate regions and the remaining Sertoli cells were undergoing apoptosis, seen through
496 caspase 3 staining (Fig. 10S). Local inflammation, or orchitis, was suggested by immune
497 infiltrates (Fig. 10R). Both the PET signal and pathology is greater in the left testicle of JF82.
498 Staining macrophages and mature spermatids for CD206 and all cells for caspase 3 activation
499 reveals a severe, acute response within short stretches of the seminiferous tubules where the
500 Sertoli cells are undergoing apoptosis due to inflammasome activation (caspase 3 activation),
501 and no spermatids are present consistent with an ongoing acute infection (Fig. 10N-S). We
502 have detected infected cells within the JF82 testes ((Fig. 10T, U) and the relationship between

503 the infected cells and testicular pathology is ongoing. Similar decreases in the cellular content
504 of the seminiferous tubules and sloughing of Sertoli cells and spermatids into the lumen have
505 been reported in multiple studies of autopsy tissues from COVID-19 related fatalities[35-40].

506 Our results suggest that SARS-CoV-2 rapidly and efficiently infects multiple tissues of the
507 male genital tract (MGT) early during infection in rhesus macaques. The complex vasculature
508 and known ACE2 expression of the tissues of the MGT make it a potential target of the virus[11,
509 41-43]. The SARS-CoV-2 infection of the testicles has been reported in mouse and hamster
510 respiratory challenge models[44-46]. Likewise, the testicles are also a target of Ebola and Zika virus
511 during systemic infection[47]. We observed a similar distribution of PET-probe signal in all 3
512 animals in the week 1 scan with labeling of the prostate, root of the penis, the top the testicles
513 and a second region of labeling at the base of the testicles (Fig. 11E-H). The signal above the
514 testicles localizes to the pampiniform plexus and vasculature of the spermatic cord while the
515 signal at the base of the testes is less clear, but appears to be associated with the cauda
516 epididymis, the highly vascularized tail of the epididymis that serves as the storage site for
517 mature sperm. A further dissection of the testicles before the organ scan should facilitate a
518 detailed localization of the PET signal associated with the MGT in future studies.

519 Although these studies were done with a rhesus macaque model, it is reasonable to
520 suggest that these observations may also apply to humans infected with SARS-CoV-2 because of
521 several clinical observations relating to male sexual health and fertility. It is highly relevant in
522 this extrapolation to consider that we have identified 4 distinct tissues where SARS-CoV-2
523 infection could impact male sexual health and fertility: SARS-CoV-2 infection of the prostate,
524 penis, pampiniform plexus, and testicles. The infection of the MGT and associated pathology

525 has been suggested by several publications and clinical studies. The prostate is known to be
526 ACE2 positive.[48] Interest in SARS-CoV-2 infection of the prostate has focused on two areas. First
527 is the potential impact on treatment of benign prostate hyperplasia[49] and prostate cancer [50]
528 with androgen deprivation therapy on the severity of COVID-19[51] and secondly, the potential
529 impact of SARS-CoV-2 infection on prostate cancer treatments. It is notable that prostate
530 cancers are known to express high levels of transmembrane serine protease 2, TMPRSS2[52],
531 which is known to activate the SARS-CoV-2 spike protein to its optimal fusogenic potential[53].
532 Multiple studies have explored this space and it does not appear that SARS-CoV-2 infection is
533 associated with an increase in prostate cancer[54]. In contrast, another study suggests that
534 infection with SARS-CoV-2 may be associated with an increase in prostate specific antigen (PSA)
535 detection in plasma[55]. Future studies are needed to confirm whether the robust signal of the
536 SARS-CoV-2 PET/CT probe reflects a high-level infection of the human prostate and its
537 subsequent impact on male sexual health and fertility[56, 57]. SARS-CoV-2 infection of the penis is
538 potentially associated with the vasculature of the corpus cavernosum, which expresses high
539 levels of ACE2 in the rhesus macaque and human penile tissue (Fig 7S) [43, 58]. Because the corpus
540 cavernosum plays a key role in erectile function, the inflammation caused by SARS-CoV-2
541 infection of the penile vasculature is hypothesized to lead to erectile dysfunction (ED). This has
542 indeed been reported to be linked to COVID-19[43, 59, 60]. In addition, treatments for ED such as
543 Viagra and Cialis are known to affect the renin-angiotensin-aldosterone-system where ACE2
544 functions as a part of the physiologic regulation of blood flow associated with normal erectile
545 function[61].

546 A potential impact of COVID-19 infection on the pampiniform plexus might be suggested
547 by several case reports of COVID-19 associated thrombosis located in the pampiniform plexus[62-
548 65]. Additionally, the signal distribution of the left and right testes is distinct, with the signal of
549 the right testicle being more focused at the top of the testicle while the signal on the left
550 testicle being more distributed in the spermatic cord. This is reminiscent of the condition
551 known as varicocele, which manifests as varicose veins of the scrotum, and is prominent in the
552 left testicle relative to the right testicle[66]. This is due to the left testicle receiving its blood flow
553 from the left renal vein which exposes it to higher blood pressure and slower blood flow[67]. This
554 difference could be insightful if it is confirmed in more animals.
555 The potential infection of the testicles by SARS-CoV-2 could be highly impactful on male
556 fertility, potentially decreasing sperm count and semen quality[47, 68-70]. It is known that SARS-
557 CoV-2 infection in humans is associated with oligo- and azoospermia and a transient decrease
558 in fertility after infection[36, 38, 66, 68, 71, 72]. One study found that fertility amongst infected men
559 was reduced and returned to baseline 3-6 months after SARS-CoV-2 infection[73]. This decrease in
560 fertility was not seen in infected women or men who received a SARS-CoV-2 vaccination. We
561 find that the pathology associated with the testicles in the week 2 necropsy is extreme, with
562 apparent ablation of sperm production within short regions of the seminiferous tubules and
563 with accompanying immune infiltration consistent with an emerging COVID-19 associated
564 orchitis[64, 74]. Multiple studies have reported a decrease in testosterone after SARS-CoV-2
565 infection[56, 75, 76]. Leydig cells, which produce testosterone, are known targets of SARS-CoV-2[35,
566 37, 77]. The decrease in testosterone correlates with disease severity[76, 78]. This susceptibility of
567 the MGT to infection with SARS-CoV-2 may be consideration in the of higher mortality

568 associated with COVID-19 in men compared to women. The direct infection of the testicles
569 observed in the NHP studies presented here are consistent with the MGT pathology reported in
570 men[35-40]. The infection of the MGT may be a common outcome in SARS-CoV-2 infection. We
571 suggest further study in mild, and even in asymptomatic infection, in men and macaques is
572 clearly required. Because of the four distinct mechanisms negatively impacting human male
573 sexual health and fertility, and the observation of all four mechanisms in all animals evaluated
574 to date, we feel compelled to report this information at this early stage of study and evaluation.
575 Using a novel ^{64}Cu-labelled F(ab')2 probe targeting the SARS-CoV-2 spike protein, we
576 have found that it is possible to identify sites of SARS-CoV-2 infection in the rhesus macaque
577 infection model using a PET/CT scan. The rapid and consistent spread of SARS-CoV-2 infection
578 to the MGT in the first week of infection in the rhesus macaque suggests this could be an
579 important post pandemic health consideration as those infected during the pandemic develop
580 advanced disease and other manifestations of long COVID-19. Currently, there is no other
581 methods that allows for the unbiased discovery of novel anatomical sites of SARS-CoV-2
582 infection. We believe the immunoPET technique described here will be an important addition
583 to the toolkit for studying and understanding SARS-CoV-2 pathogenesis. The availability of an
584 immunoPET probe to SARS-CoV-2 in the clinical setting has the potential to reveal the
585 underlying role of disseminated viral infection in long COVID and could guide therapeutic
586 interventions to resolve SARS-CoV-2 related sequalae which could be a major health concern
587 for the lifetimes of those infected during the COVID-19 pandemic.
588

589 **ACKNOWLEDGEMENTS:** This work was supported by a NOSI supplement (R37AI094595-10S1 PI:
590 Hope) to parent grant R37AI094595 (PI Hope) and by NIH grants R21AI163912 (PI Hultquist)
591 P51OD01110459, and U19AI135964 (E.A.O.). We would like to thank Nicholas Maness for
592 supplying the delta variant virus and Maury Duplantis, Brooke F. Gasperge, Kasi E. Russell-
593 Lodrigue, and the Veterinary team at TNPRC. Thanks to Rich D'Aquila for critical reading and
594 editing of the manuscript.

595

596

597 **Material and Methods**

598 **Preparation of F(ab)2**

599 CR3022-IgG1 was acquired from Absolute Antibody (#Ab01680-10.0, Absolute Antibody). The
600 IgG1 was digested into F(ab)2 as previously described. Briefly, a Genovis FragIT antibody
601 digestion kit (#A2-FR2-100, Genovis) was used according to manufacturer's protocol. CR3022
602 was digested by adding to the FragIT column and rocking for 1 hr. at room temperature. The
603 column was then centrifuged to elute fragments. Fc fragments were removed after incubation
604 with the CaptureSelect Fc Column. F(ab')2 fragments were eluted from this column and size
605 was confirmed using SDS-PAGE.

606

607 **DOTA Labeling of Antibody**

608 CR3022-F(ab)2 was labeled with the chelator dodecane tetra-acetic acid (DOTA) for the
609 attachment of ^{64}Cu. Chelex 100 chelating resin (#142-1253, BioRad) was used to prepare two
610 buffers: 0.1M sodium phosphate (pH 7.3) and 0.1M ammonium acetate (pH 5.5). Five grams of

611 Chelex was added to 100ml of each buffer and stirred at room temperature for 1 hour. Buffers
612 were then filter sterilized using 0.22 µM filters. CR3022-F(ab')2 was buffer exchanged into the
613 prepared 0.1 M sodium phosphate using Zeba columns (ThermoFisher, USA). DOTA-NHS-ester
614 (#B-280, Macrocyclics) was dissolved in dimethyl sulfoxide (DMSO) at a concentration of 10mM.
615 A 1:10 dilution of 1M sodium bicarbonate was made into a tube containing F(ab')2 in sodium
616 phosphate and 10mM DOTA was added at a molar ratio of 5:1. The tube was mixed and left to
617 rock at 37C for 1.5 hours. The labeled F(ab')2 was then buffer exchanged into fresh 0.1 M
618 sodium phosphate using a Zeba column.
619
620 **^{64}Cu labeling**
621 Before labeling DOTA conjugated F(ab')2 was buffer exchanged into freshly prepared 0.1M
622 ammonium acetate (pH 5.5) prepared with Chelex 100 using 10kDa cutoff Amicon centrifugal
623 microfilters (Cork, IRL). Cu^{64} chloride was obtained from Washington University, St. Louis MO
624 and shipped overnight to TNPRC. All work with Cu^{64} was performed inside a lead castle. The
625 radioactivity of the Cu^{64} was measured using an Atom Force 500 dose calibrator and recorded.
626 Next the Cu^{64} was added to a tube containing the DOTA labeled F(ab')2 in 0.1 M ammonium
627 acetate and incubated at 37°C for 1 hour while rotating. The labeled F(ab')2 probe was then
628 separated from unlabeled Cu^{64} and buffer exchanged into PBS via sequential centrifugation
629 steps using 10kDa cutoff Amicon centrifugal microfilters to a final volume of ~20µl. The
630 conjugated probe was then diluted to the final volume in PBS in sterile glass vials and drawn
631 into single dose syringes. Each dose typically labelled in the 1-3 mCi per dose.
632

633 **Animals and virus**

634 The virus used for experimental infection of LP14 was SARS-CoV-2; 2019-nCoV/USA-WA1/2020
635 (*https://www.ncbi.nlm.nih.gov/nuccore*; accession number MN985325.1) obtained from BEI
636 resources (BEI #NR-52281). Virus stock was prepared in Vero E6 cells and sequence confirmed
637 by deep sequencing. Plaque assays were performed in Vero E6 cells. Vero E6 cells were
638 acquired from ATCC (Manassas, VA). The virus used for experimental infection of IN22 and JF82
639 was SARS-CoV-2; hCoV-19/USA/MD-HP05647/2021 (Lineage B.1.617.2; Delta variant) obtained
640 from BEI resources (BEI #NR-55672). Delta variant stock was expanded using Calu-3 cells and
641 prepared as above using Vero E6 cells.

642 Three male rhesus macaques (Macaca mulatta) were used in this study. All animals were
643 housed at the Tulane National Primate Research Center (TNPRC, Covington, LA) which is
644 accredited by the Association for the Assessment and Accreditation of Laboratory Animal Care.
645 All procedures were reviewed and approved by the Tulane University Institutional Animal Use
646 Committee under protocol number P0452.One animal was inoculated with $1.1x10^6$ tissue
647 culture infectious dose ($TCID_{50}$) of the WA1 strain of SARS-CoV-2 via concomitant
648 intratracheal/intranasal instillation (1mL intratracheal, 500µL per each nare). This animal was
649 necropsied 8 days post-infection. The remaining two animals were inoculated with $1.12x10^6$
650 $TCID_{50}$ of the delta variant of SARS-CoV-2 via the same route. One animal was necropsied at day
651 7 and one at day 14 post-infection. All animals were intravenously infused with 0.5 mg/kg of
652 the radiolabeled F(ab')2 probe and JF82 was infused on two separate occasions. Macaque LP14
653 received 4 mCi, JF82 and IN22 received 1.3 and 1,4 mCi respectively on Dec 9, and JF82 received
654 an additional dose of 0.7 mCi on Dec 15. LP14 had nasal and salivary swabs taken at day 7. IN22

655 had swabs taken at days 3, 5, and 7 post-infection, while JF82 had swabs taken at days 3, 5, 7,
656 and 14.
657
658 **PET/CT Imaging and Necropsy**
659 PET/CT guided necropsies were performed in three sequential phases each separated by a
660 PET/CT followed by a period of analysis and sampling (1. whole-body, 2. organ, and 3. tissue).
661 First, whole-body scans were acquired prior to sending the animal to necropsy. Following
662 euthanasia, all major organ systems were removed (pluck, gastrointestinal tract, liver, spleen,
663 kidneys, urinary bladder, testicles, penis, prostate, seminal vesicles, nasal turbinate, lymph
664 nodes, carotid artery, cervical spinal cord, and brain) placed in a clear, plastic, sealable
665 container and sent back to PET/CT for an "organ scan". After the organ scans were
666 reconstructed, "hot" regions of each major organ (as seen on the organ scan) were sampled
667 and placed in cryomolds. The final "tissue" scan was acquired by placing the cryomolds in a
668 clear, plastic, sealable container and scanning them with the PET/CT. Following acquisition of
669 the tissue scan, cryomolds were filled with OCT and frozen on dry ice. All remaining tissue (not
670 placed in cryomolds) was placed in zinc-formalin fixative. All samples were stored for 5 days
671 before being removed from containment.
672
673 **PET/CT Image Analysis**
674 Acquired PET/CT whole-body images were analyzed using the MIM Software (MIM Software
675 Inc., Cleveland, OH). The PET and CT scans were reconstructed using the software and PETCT
676 fusions were created to analyze regions of interest through axial, sagittal, and coronal views.

677 The PET scans were presented in calculated Standardized Uptake Values, and all images were
678 set to the same scale (0-20 SUVbw). The PET scale was selected based on the overall signal
679 intensity of the PET scans, and the CT scale for optimal visibility of the tissues. Regions of
680 interest (ROI) were isolated using a combination of the Region Grow function and manual
681 contouring on a representative scan, then these regions were copied on subsequent scans of
682 the same animal using a specialized developed workflow. This workflow allows the software to
683 use the CT scans to map the selected ROI and locate that exact volume in subsequent scans.
684 Manual adjustments were then used to counter any changes in the animals' orientation
685 between scans. The areas within these regions were then extracted from the full scans, and the
686 anatomical regions were analyzed in both 2D cross-sections and 3D projections. 3D views are
687 maximum intensity projections of isolated ROI in the PET scans.
688 To cluster tissues according to their SUV signal characteristics, we used Principal Component
689 Analysis (PCA) where we included all variables obtained from the SUV measurements (i.e., Total
690 SUV, Total SUV Whole Body ratio, Mean SUV, Median SUV, Standard Deviation SUV, Max SUV,
691 and Kurtosis) for each tissue and animal. The clustering of each tissue was subsequently
692 obtained by agglomerative hierarchical clustering on the PCA results. After building an initial
693 hierarchical tree, the sum of within-cluster inertia was calculated for each partition. The
694 selected partition was the one with the higher relative loss of inertia. Both PCA and
695 agglomerative hierarchical clustering were performed using FactoMineR package and
696 Factoextra was used for visualization of the clustering results.
697
698 **Isolation and Quantification of viral RNA**

699 Viral load was quantified from pharyngeal and nasal swabs taken from infected animals at
700 TNPRC as previously described (1) Swab and bronchial brush samples were collected in 200 µL
701 of DNA/RNA Shield 1× (catalog number R1200; Zymo Research, Irvine, CA) and extracted for
702 viral RNA using the Quick-RNA viral kit (catalog number R1034/5; Zymo Research). The Viral
703 RNA Buffer was dispensed directly to the swab in the DNA/RNA Shield. A modification to the
704 manufacturers' protocol was made to insert the swab directly into the spin column to
705 centrifugate, allowing all the solution to cross the spin column membrane. The viral RNA was
706 then eluted (45 µL) from which 5 µL was added in a 0.1-mL fast 96-well optical microtiter plate
707 format (catalog number 4346906; Thermo Fisher Scientific, Waltham, MA) for a 20-µL real-time
708 quantitative RT-PCR (RT-qPCR) reaction. The RT-qPCR reaction used TaqPath 1-Step Multiplex
709 Master Mix (catalog number A28527; Thermo Fisher Scientific) along with the 2019-nCoV RUO
710 Kit (catalog number 10006713; IDTDNA, Coralville, IA), a premix of forward and reverse primers
711 and a FAM-labeled probe targeting the N1 amplicon of the N gene of SARS2-nCoV19
712 (https://www.ncbi.nlm.nih.gov/nuccore; accession number MN908947). The reaction master
713 mix was added using an X-stream repeating pipette (Eppendorf, Hauppauge, NY) to the
714 microtiter plates, which were covered with optical film (catalog number 4311971; Thermo
715 Fisher Scientific), vortexed, and pulse centrifuged. The RT-qPCR reaction was subjected to RT-
716 qPCR at a program of uracil-DNA glycosylase incubation at 25°C for 2 minutes, room
717 temperature incubation at 50°C for 15 minutes, and an enzyme activation at 95°C for 2 minutes
718 followed by 40 cycles of a denaturing step at 95°C for 3 seconds and annealing at 60°C for 30
719 seconds. Fluorescence signals were detected with a QuantStudio 6 Sequence Detector (Applied
720 Biosystems, Foster City, CA). Data were captured and analyzed with Sequence Detector

721 Software version 1.3 (Applied Biosystems). Viral copy numbers were calculated by plotting Cq
722 values obtained from unknown (i.e., test) samples against a standard curve that represented
723 known viral copy numbers. The limit of detection of the viral RNA assay was 10 copies per
724 reaction volume. A 2019-nCoV–positive control (catalog number 10006625; IDTDNA) was
725 analyzed in parallel with every set of test samples to verify that the RT-qPCR master mix and
726 reagents were prepared correctly to produce amplification of the target nucleic acid. A non-
727 template control was included in the qPCR to ensure that there was no cross-contamination
728 between reactions.
729 OCT embedded tissue blocks were sectioned between 10-15 µM and 2-4 sections were
730 placed into RNAse free tubes. RNA extraction was carried out using a RNeasy Plus Mini Kit
731 (#74124, Qiagen), according to manufacturer's protocol. Briefly, 350ul of lysis buffer with
732 dithiothreitol (DTT) was added to the tubes containing sections. The tubes were vortexed
733 briefly then frozen at -20C. Once thawed the samples were again vigorously vortexed then
734 centrifuged for 3 minutes. Supernatant was removed and applied to the gDNA Eliminator spin
735 column. The flow-through was mixed with 350ul of 70% ethanol and added to a RNeasy spin
736 column. The spin column was washed three times with buffers RW1 and RPE. RNA was then
737 eluted using 30-50ul of RNAse free water. All steps prior to addition of lysis buffer were carried
738 out in a BSL3 facility.
739
740 **Tissue Processing and H&E Staining**
741 Tissue samples were collected in Zinc formalin (Anatech) and fixed for a minimum of 72 hours
742 before being washed and dehydrated using a Thermo Excelsior AS processor. Upon removal

743 from the processor, tissues were transferred to a Thermo Shandon Histocentre 3 embedding
744 station where they were submersed in warm paraffin and allowed to cool into blocks. From
745 these blocks, 5um sections were cut and mounted on charged glass slides, baked overnight at
746 60°C, and passed through Xylene, graded ethanol, and double distilled water to remove paraffin
747 and rehydrate tissue sections. A Leica Autostainer XL was used to complete the
748 deparaffinization, rehydration and routine hematoxylin and eosin stain. Slides were digitally
749 imaged with a NanoZoomer S360 (Hamamatsu) and subsequently examined by a board-
750 certified, veterinary pathologist using HALO software (Indica Labs).
751
752 **Fluorescent Immunohistochemistry of FFPE tissues**
753 5um sections of Formalin-fixed, paraffin-embedded (FFPE) tissues were mounted on charged
754 glass slides, baked for two hours at 60°C, and passed through Xylene, graded ethanol, and
755 double distilled water to remove paraffin and rehydrate tissue sections. A microwave was used
756 for heat induced epitope retrieval. Slides were heated in a high pH solution (Vector Labs H-
757 3301), rinsed in hot water, and transferred to a heated low pH solution (Vector Labs H-3300)
758 where they were allowed to cool to room temperature. Sections were washed in a solution of
759 phosphate-buffered saline and fish gelatin (PBS-FSG) and transferred to a humidified chamber,
760 for staining at room temperature. Lung sections were blocked with 10% normal goat serum
761 (NGS) for 40 minutes, followed by a 60-minute incubation with the anti-SARS primary antibody
762 diluted in NGS. Slides were washed and transferred back to the humidified chamber for a 40-
763 minute incubation with the secondary antibody, also diluted in NGS. Sequential staining of FFPE
764 testes, for CD206 and Caspase 3, was done as described above with 1% normal donkey serum

765 (NDS) being used in place of NGS for blocking and antibody dilutions. DAPI was used to label the
766 nuclei of each section. Slides were mounted using a homemade anti-quenching mounting
767 media containing Mowiol (Calbiochem #475904) and DABCO (Sigma #D2522) and imaged at
768 20X with a Zeiss Axio Slide Scanner.
769

PRIMARY ANTIBODY	SPECIES	COMPANY	CATALOG	DILUTION	SECONDARY ANTIBODY
SARS	Guinea Pig	BEI	NR-10361	1:1000	Goat anti-guinea pig Alexa Fluor488
CD206	Goat	R&D Systems	AF2532	1:50	Donkey anti-goat Alexa Fluor488
Caspase 3	Rabbit	Abcam	Ab13847	1:200	Donkey anti-rabbit Alexa Fluor555
DAPI		Invitrogen	D1306	1:20,000	

770

771 **Fluorescence Microscopy of OCT embedded tissues**

772 OCT embedded tissue were cryosectioned in a BSL3 facility between 10 and 15 µM. One or two
773 sections of each tissue were placed on glass microscope slides. Tissues were placed into an
774 airtight container containing 4% PFA in PIPES buffer. The container was sealed and thoroughly
775 decontaminated before being removed from the BSL3 facility. The remainder of the staining
776 took place outside of the BSL3. Tissue sections were treated with L-lysine (0.1%, SigmaAldrich)
777 to reduce background and non-specific interactions before being blocked using 3% BSA
778 (Invitrogen, ThermoFisher) for 30 minutes at room temperature. Staining with primary
779 antibodies was carried out at 37°C and secondary antibodies at room temperature. each for
780 1hr. Table of primary and secondary antibodies used is below. All slides were stained with

781 Hoechst (1:25,000, ThermoFisher, USA) for 15 minutes and washed with PBS between all steps.
782 Dako fluorescent mounting medium (#S302380-2, Agilent, USA) was used to mount cover slips
783 which were sealed with nail polish. A DeltaVision Ultra inverted microscope (Cytivia, USA) was
784 used to obtain images using the 10x, 20x, 60x, and 100x lenses. Images were deconvolved,
785 stitched, and projected using the softWoRx software (Applied Precision, USA).

Clone	Antibody	Target	Company	Catalog#	Dilution
	Rb pAb	Spike	Abcam	Ab272504	1:200
3A2	Ms mAb	Spike	Abcam	Ab272420	1:200
6H3	Ms mAb	NC	GeneTex	GTX632269	1:200
5A10	Ms mAb	NSP8	GeneTex	GTX632696	1:200
	Rb pAb	NC	Novus Biologicals	NB100-56576	1:200
	Rb pAb	NC	GeneTex	GTX135357	1:200
rJ2	Ms mAb j2	Anti-double stranded RNA	Millipore Sigma	MABE1134	1:1000

786

787

788

789 **Figure 1**. Study design and viral analysis of infected macaques. (A) Workflow of PET/CT guided
790 necropsy. (B) Schematic showing the study design of probe administration, PET/CT scans, and
791 infection. (C-E) Lung lesions were consistent with prior findings in NHPs infected with SARS-
792 CoV-2 and varied from minimal in LP14 (C), moderate in IN22 (D), and mild in JF82 (E). Insets
793 demonstrate the inflammatory infiltrate and in IN22 and JF82, type II pneumocyte hyperplasia
794 (arrows). (F and G) Viral load measurements for all three animals. (F) shows copies/swab of
795 genomic N while (G) shows copies/swab of subgenomic N.

796

797 **Figure 2.** LP14 PET/CT guided necropsy. (A and B) Whole-body PET/CT scans of LP14 8 days
798 post-infection. Front view (A) and rotated 45° (B) both shown. PET signal is display as SUV. (C)
799 Post necropsy PET/CT organ scan of LP14. (D and E) Images of tissues scanned in (C). (F) Overlay
800 of PET signal onto photograph of small pieces of tissue in cassettes. (G and H) Lung PET signal
801 was isolated and overlaid on whole body CT scans. Side (G) and front (H) view. (I and J) Isolated
802 lung PET volumes used in G and H are shown independently, side view (I) and front view (J). (K
803 and L) Single axial z-slice images of respiratory tract PET/CT signals are shown, each image
804 represents a single z-plane from scan shown in C. (M and N) Fluorescent microscopy images of
805 LP14 lung tissue blocks. Red is SARS-CoV-2 anti-sera and blue is Hoechst nuclear stain. Scale
806 bars 100 µM (M) and 25 µM (N).
807
808 **Figure 3.** Male genital tract signal in LP14. (A, B, and C) PET/CT images highlighting the lower
809 abdomen of LP14 from the whole-body scan. Front (A) rotated 45° (B), and side (C) views are all
810 shown. Right and left labeled in front view. Red arrow in B and C shows location of baculum in
811 CT scan. (D and E) PET signal with CT overlay removed to highlight signal in MGT, front (D) and
812 side (E) views shown. (F, H, and J) Isolated 3D volume of MGT from whole body scan overlaid
813 with CT images. Side (F) rotated 45° (H), and front (J) views shown. (G, I, and K) Isolated 3D
814 volume of MGT used in overlays (F, H, and J) shown with same views. (L) Overlay of single z-
815 plane of PET signal from organ scan onto image of testis of LP14. (M) PET signal from single z-
816 plane of organ scan used in (L). (N) Image of LP14 testis used in (L). (O) 3D volume of PET signal
817 from organ scan of single testis in previous panels.
818

819 **Figure 4.** Immunofluorescence of LP14 Testes. (A) Fluorescent microscopy image of LP14
820 seminiferous tubules. ACE2 staining shown in red, Hoechst nuclear staining shown in blue. Inset
821 shows zoom in of single tubule to better view ACE2 staining in Sertoli and myeloid cells. Scale
822 bars 50 µM. (B) Fluorescent microscopy image of LP14 testis shows infected cells. SARS-CoV-2
823 anti-sera staining in green, background fluorescent in red, and Hoechst nuclear staining in blue.
824 Scale bars 25 µM. (C) Microscopy images of two tubules containing infected cells (top and
825 bottom rows). Red is SARS-CoV-2 anti-sera, green is smooth muscle actin, gold is vimentin, and
826 blue is Hoechst nuclear stain. Possible infected germ cells based on morphology and localization
827 and marked by arrow heads. Scale bars 20 µM.
828
829 **Figure 5.** IN22 PET/CT guided necropsy images. (A and B) Whole-body PET/CT scans of IN22
830 obtained 3-hours after probe administration. Front view (A) and side (B) both shown. (C and D)
831 Whole-body PET/CT scans of IN22 obtained 21-hours after probe administration. Front view (C)
832 and side (D) both shown. Right and left labeled in front views (A and C). (E) Organ tray post
833 necropsy and (F) PET/CT image. (G) Second organ tray post necropsy and (H) PET/CT image. (I)
834 Overlay of PET signal onto photograph of tissue cassettes.
835
836 **Figure 6.** IN22 lung pathology and PET signal. (A-D) Lung PET volumes were isolated and
837 overlaid on whole body CT scans. (A and B) Show lung volumes from 3-hour scan, side (A) and
838 front (B) views shown. (C and D) Show lung volumes from 21-hour scan, side (C) and front (D)
839 views shown. (E and F) Isolated lung PET volumes for each scan are shown independent of CT.
840 (G) Sagittal z-slice from CT showing lungs. (H) PET signal overlaid on z-slice from G. (I)

841 Transverse z-slice through torso from CT. (J) PET signal overlaid on z-slice from I. (K) Image of
842 respiratory tract after necropsy. (L) Inset showing overt lung pathology in right lower lobe. (M)
843 PET/CT signal from organ scan of respiratory tract. (N) PET/CT signal from M overlaid onto
844 image from K. (O) PET/CT signal with CT contrast increased to observe pathology in lower right
845 lung lobe. (P) H&E image of lung tissue showing areas of expanded alveolar space and
846 inflammatory infiltrate (arrows). (Q) Immunofluorescence image of the same tissue from P.
847 Green is SARS-CoV-2 anti-sera, red is background, and white is nuclear stain. White arrows
848 indicate SARS-CoV-2 positive cells. (R) H&E image of lung tissue showing macrophages and
849 neutrophils (arrowheads) and type II pneumocytes (arrows). (S) Immunofluorescence image
850 showing infected cells of the alveoli (arrows) and lining the alveolar septa (arrowheads). Green
851 is SARS-CoV-2 anti-sera, red is background, white is nuclear stain. All scale bars are 100 µM. (T)
852 Fluorescent microscopy image of IN22 lung tissue. Spike shown in green, nucleocapsid shown in
853 red, background in white, and Hoechst nuclear stain in blue. Scale bar 100 µM. (U, Y, W)
854 Additional fluorescent microscopy images of lung tissue showing foci of infected cells. U and W
855 are shown in low magnification Y. Green is SARS-CoV-2 anti-sera and blue is Hoechst nuclear
856 stain. Scales bar 500 µM. (X-Z) Validation of dual antibody staining utilizing spectral imaging. (X)
857 shows microscopy of J2 antibody with RedX secondary and rabbit anti-NC monoclonal () and
858 Cy5 secondary. (Y) Shows area within green square in X. White arrows point to regions of
859 interest that are cell associated. Grey arrows indicate control regions of spectral evaluation.
860 The areas evaluated by spectral imaging in (Y) are color coded and match with the spectra
861 shown in (Z).
862

863 **Figure 7.** Male genital tract signal in IN22. (A and B) PET/CT images highlighting the lower
864 abdomen of IN22 obtained 3-hours after probe administration. Front view (A) and side (B) both
865 shown. (C and D) PET/CT images highlighting the lower abdomen of IN22 obtained 21-hours
866 after probe administration. Front view (C) and side (D) both shown. (E and F) Isolated 3D
867 volume of MGT from 3-hour scan overlaid with whole-body CT. Side (E) and front (F) views
868 shown. (G and H) Isolated 3D volume of MGT from 21-hour scan overlaid with whole-body CT.
869 Side (G) and front (H) views shown. (I and J) Whole-body CT images of lower abdomen, red
870 contours outline the testicles and spermatic cords. Front (I) and side (J) views shown. (K and L)
871 3D volume of MGT overlaid onto CT images from previous panels. (M) Image of testicles after
872 necropsy. (N) PET signal from organ scan of testicles. (O) Overlay of PET signal onto image from
873 panel M. (P) Overlay of PET signal onto CT signal from same scan. White asterisks mark location
874 of pampiniform plexus in all previous panels. (Q and R) Fluorescence microscopy of SARS-CoV-2
875 infected cells in testicular tissue from IN22. Red is SARS-CoV-2 spike, green is SARS-CoV-2
876 nucleocapsid, white is background, and blue is Hoechst nuclear stain. Insets show channels
877 independently, larger image is all channels merged. Scale bars 10 µM (S) Fluorescent
878 microscopy image of corpus cavernosum tissue from an uninfected animal showing ACE2
879 staining in red, background in green, and Hoechst nuclear staining in blue. Scale bar 100 µM (T)
880 Fluorescence microscopy of SARS-CoV-2 infected cells in penile tissue from IN22. White is
881 dsRNA antibody J2, red is SARS-CoV-2 nucleocapsid, green is background, and blue is Hoechst
882 nuclear stain. (U, V, and W) Show individual cells highlighted in T.
883

884 **Figure 8.** JF82 PET/CT images from week and week 2 necropsy scans. (A and B) Whole-body
885 PET/CT scan of JF82 from 1-week post-infection. Front view (A) and side (B) both shown. (C and
886 D) Whole-body PET/CT scans of JF82 2-weeks post infection. Front view (C) and side (D) both
887 shown. Right and left labeled in front views (A and C). (E and F) Overlay of the week 1 scan
888 (shown in red) and the week 2 scan (shown in blue). Front (E) and side (F) views both shown.
889 (G) Organ tray post necropsy and (H) PET/CT image. (I) Second organ tray post necropsy and (J)
890 PET/CT image. (K) Overlay of PET signal onto photograph of tissue cassettes.
891
892 **Figure 9.** JF82 lung pathology and PET signal from two timepoints. (A-D) Lung PET volumes were
893 isolated and overlaid on whole body CT scans. (A and B) Show lung volumes from 1-wee scan,
894 side (A) and front (B) views shown. White asterisk indicates location of lung pathology
895 highlighted below. (C and D) Show lung volumes from 2-week scan, side (C) and front (D) views
896 shown. (E and F) Isolated lung PET volumes for each scan are shown independent of CT. (G and
897 H) Overlay of single z-image of PET signal onto single z-image of CT in the lungs at week 1 (G)
898 and week 2 (H). (I and J) Single z-image of CT used in G and H shown independent of PET signal
899 for week 1 (I) and week 2 (J). (K) Overlay of week 1 (shown in red) and week 2 (shown in blue)
900 PET signal. (L) Overlay from K shown with CT image to localize PET signal. Insets above show,
901 CT, week 1, and week 2 signal from left to right. White asterisk indicates location of left lung
902 pathology in all panels.
903
904 **Figure 10.** Male genital tract signal in JF82. (A and B) Front view PET/CT images highlighting the
905 lower abdomen of JF82 at 1-week (A) and 2-weeks (B). (C) Overlay of week 1 (shown in red) and

906 week 2 (shown in blue) PET signal. (D and E) Side view of same images shown in A and B. (F)
907 side view of overlay shown in C. (G and H) Isolated MGT volume from week 1 scan. Back (G) and
908 side (H) views shown. (I and J) Isolated MGT volume from week 2 scan. Back (I) and side (J)
909 views shown. (K, L, and M) Isolated MGT volume from week 2 with isolated penile and
910 testicular signal. Back (K), rotated 45° (L), and side (M) views shown. (N) H&E stain of JF82
911 testicular tissue. Degenerate seminiferous tubules highlighted in black oval. Scale bar 500 µM.
912 (O) Fluorescent microscopy shows a similar area of degenerate tubules. Green is CD206, red
913 caspase 3, and white nuclear stain. Scale bar 500 µM. (P) Higher magnification image of
914 degenerate tubules. Intraluminal macrophages (arrowheads) and Sertoli cells (arrows) are
915 shown inside tubules. Scale bar 50 µM (Q) Higher magnification of image in O shows Sertoli
916 cells (arrow) staining with caspase 3 and macrophages (arrowhead) staining with CD206. Scale
917 bar 50 µM. (R) Fluorescent microscopy image showing degenerate tubule full of intraluminal
918 macrophages. Red is caspase 3, green is CD206, and blue is nuclear stain. Scale bar 50 µM. (S)
919 Lower magnification microscopy image of degenerate and healthy tubules. Red is caspase 3,
920 green is CD206, and blue is nuclear stain. Scale bar 200 µM. (T and U) Fluorescent microscopy
921 images of infected cells in testicular tissue of JF82. White is SARS-CoV-2 anti-sera, red is NSP8,
922 green is nucleocapsid, and blue is Hoechst nuclear stain. Insets show individual channels, larger
923 image is merge. Scale bars 10 µM.
924
925 **Figure 11.** Comparison of SUVs across animals and timepoints. (A-D) Complete rotation series of
926 lung PET volumes for LP14 (A), IN22 (B), JF82 week 1 (C), and JF82 week 2 (D). (E-H) Front,
927 rotated 45°, and side views of MGT PET volumes for LP14 (E), IN22 (F), JF82 week 1 (G), and

928 JF82 week 2 (H). (I-K) Front and side views of whole-body scans, white lines indicate volumes
929 taken for heart and lungs for LP14 (I), IN22 (J), and JF82 week 1 (K). Insets show each image
930 without white outlines. (L) Total SUVs for whole-body scans and each individual volume isolated
931 displayed in graph. Animals are indicated by icon shape and volumes by color.
932
933 **Figure 12.** Comparison of prostate and penile signal between animals. (A-F) PET/CT signal in
934 lower abdomen for each animal at 1-week post-infection. LP14 front (A) and rotated 45° (B),
935 IN22 front (C) and rotated 45° (D), JF82 front (E) and rotated 45° (F). Asterisks mark location of
936 prostate. Insets show sagittal z-slice of each animal highlighting prostate signal (white circle).
937 (G-I) PET/CT volume of penis for IN22. Front (G) rotated 45° (H), and side (I) views shown. (J-L)
938 PET/CT volume of penis for JF82 at 2-weeks post-infection. Front (J) rotated 45° (K), and side (L)
939 views shown. (M) PET/CT signal of IN22 penis after necropsy. (N) PET/CT signal of JF82 penis
940 after necropsy. (O) PET/CT signal overlaid onto an image of tissue cassettes (P) containing
941 penile tissue of IN22. (Q) PET/CT signal overlaid onto an image of tissue cassettes (R) containing
942 penile tissue of JF82. (S-U) H&E images of testicular tissue from each animal. LP14 (S) and IN22
943 (T) shows normal spermatogenesis and tissue architecture. IN22 (U) shows degenerate tubules
944 (asterisks) interspersed among healthy tubules. Scale bars all 500 μM.
945
946 **Figure 13.** PET signal associated with the pampiniform plexus. (A) Labeled dissection showing
947 anatomical structure of a macaque testis. (B) CT image of testes and associated image showing
948 the matching anatomical features of the spermatic cord. (C) Inset highlighting the location and
949 appearance of the pampiniform plexus. White asterisks mark the vas deferens in all images. (D-

950 F) Single z PET/CT images of IN22 highlighting the PET signal associated with the pampiniform
951 plexus (yellow volume) from the frontal (D), sagittal (E), and transverse (F) plane. (G) CT image
952 used in E to highlight signal associated with pampiniform plexus (yellow volume). (H-L) Isolated
953 3D volumes of MGT PET signal shown from the front for IN22 (H), JF82 (J), and LP14 (L). White
954 circles outline testes. (I, K, M) Volumes from H, J, and L rotated 45°. (N) Sagittal z-slice of PET/CT
955 of LP14 showing right testis. (O) Frontal z-slice of PET/CT, colored lines correspond to sagittal
956 slices shown in N, P, and R. (P) Sagittal z-slice of PET/CT showing penile tissue. (Q) Frontal z-slice
957 highlighting the testicular tissue in white ovals. (R) Sagittal z-slice of PET/CT showing left testis
958 of LP14. White ovals highlight signal associated with testes and not pampiniform plexus.
959
960 **Figure 14.** Principle components analysis of SUV measures. (A) Mean SUV values from isolated
961 tissue volumes. (B) The ratio of total SUV for each tissue volume to whole-body total SUV. (C)
962 Heat map showing clustering of tissues and parameters measured from the PET data. (D)
963
964 **REFERENCES**

965 1. Cheung CCL, Goh D, Lim X, Tien TZ, Lim JCT, Lee JN, Tan B, Tay ZEA, Wan WY, Chen EX,
966 Nerurkar SN, Loong S, Cheow PC, Chan CY, Koh YX, Tan TT, Kalimuddin S, Tai WMD, Ng JL, Low
967 JG-H, Yeong J, Lim KH. Residual SARS-CoV-2 viral antigens detected in GI and hepatic tissues
968 from five recovered patients with COVID-19. Gut. 2021. doi: 10.1136/GUTJNL-2021-324280.
969 2. Kariyawasam JC, Jayarajah U, Riza R, Abeysuriya V, Seneviratne SL. Gastrointestinal
970 manifestations in COVID-19. Trans R Soc Trop Med Hyg. 2021;115(12):1362-88. doi:
971 10.1093/trstmh/trab042. PubMed PMID: 33728439; PMCID: PMC7989191.
972 3. Keshavarz P, Rafiee F, Kavandi H, Goudarzi S, Heidari F, Gholamrezanezhad A. Ischemic
973 gastrointestinal complications of COVID-19: a systematic review on imaging presentation. Clin
974 Imaging. 2021;73:86-95. Epub 20201208. doi: 10.1016/j.clinimag.2020.11.054. PubMed PMID:
975 33341452; PMCID: PMC7837247.
976 4. Javadekar NS. Gut in COVID 19-is it worth noticing. Ind Psychiatry J. 2021;30(Suppl
977 1):S267-S9. Epub 20211022. doi: 10.4103/0972-6748.328826. PubMed PMID: 34908706;
978 PMCID: PMC8611584.

979 5. Paterson BJ, Durrheim DN. Wastewater surveillance: an effective and adaptable
980 surveillance tool in settings with a low prevalence of COVID-19. Lancet Planet Health.
981 2022;6(2):e87-e8. doi: 10.1016/S2542-5196(22)00009-2. PubMed PMID: 35150632; PMCID:
982 PMC8828367.
983 6. Gregory DA, Wieberg CG, Wenzel J, Lin CH, Johnson MC. Monitoring SARS-CoV-2
984 Populations in Wastewater by Amplicon Sequencing and Using the Novel Program SAM Refiner.
985 Viruses. 2021;13(8). Epub 20210819. doi: 10.3390/v13081647. PubMed PMID: 34452511;
986 PMCID: PMC8402658.
987 7. Nakamura Y, Katano H, Nakajima N, Sato Y, Suzuki T, Sekizuka T, Kuroda M, Izutani Y,
988 Morimoto S, Maruyama J, Koie M, Kitamura T, Ishikura H. SARS-CoV-2 is localized in
989 cardiomyocytes: a postmortem biopsy case. Int J Infect Dis. 2021;111:43-6. Epub 20210809. doi:
990 10.1016/j.ijid.2021.08.015. PubMed PMID: 34384897; PMCID: PMC8351278.
991 8. Lei J, Liu Y, Xie T, Yao G, Wang G, Diao B, Song J. Evidence for residual SARS-CoV-2 in
992 glioblastoma tissue of a convalescent patient. Neuroreport. 2021;32(9):771-5. doi:
993 10.1097/WNR.0000000000001654. PubMed PMID: 33994523.
994 9. Song E, Zhang C, Israelow B, Lu-Culligan A, Prado AV, Skriabine S, Lu P, Weizman OE, Liu
995 F, Dai Y, Szigeti-Buck K, Yasumoto Y, Wang G, Castaldi C, Heltke J, Ng E, Wheeler J, Alfajaro MM,
996 Levavasseur E, Fontes B, Ravindra NG, Van Dijk D, Mane S, Gunel M, Ring A, Kazmi SAJ, Zhang K,
997 Wilen CB, Horvath TL, Plu I, Haik S, Thomas JL, Louvi A, Farhadian SF, Huttner A, Seilhean D,
998 Renier N, Bilguvar K, Iwasaki A. Neuroinvasion of SARS-CoV-2 in human and mouse brain. J Exp
999 Med. 2021;218(3). doi: 10.1084/jem.20202135. PubMed PMID: 33433624; PMCID:
1000 PMC7808299.
1001 10. Hanley B, Naresh KN, Roufosse C, Nicholson AG, Weir J, Cooke GS, Thursz M, Manousou
1002 P, Corbett R, Goldin R, Al-Sarraj S, Abdolrasouli A, Swann OC, Baillon L, Penn R, Barclay WS,
1003 Viola P, Osborn M. Histopathological findings and viral tropism in UK patients with severe fatal
1004 COVID-19: a post-mortem study. Lancet Microbe. 2020;1(6):e245-e53. Epub 20200820. doi:
1005 10.1016/S2666-5247(20)30115-4. PubMed PMID: 32844161; PMCID: PMC7440861.
1006 11. Edenfield RC, Easley CAt. Implications of testicular ACE2 and the renin-angiotensin
1007 system for SARS-CoV-2 on testis function. Nat Rev Urol. 2022;19(2):116-27. Epub 20211126.
1008 doi: 10.1038/s41585-021-00542-5. PubMed PMID: 34837081; PMCID: PMC8622117.
1009 12. Collins AB, Zhao L, Zhu Z, Givens NT, Bai Q, Wakefield MR, Fang Y. Impact of COVID-19
1010 on Male Fertility. Urology. 2022. doi: 10.1016/J.UROLOGY.2021.12.025.
1011 13. Parker AM, Brigham E, Connolly B, McPeake J, Agranovich AV, Kenes MT, Casey K,
1012 Reynolds C, Schmidt KFR, Kim SY, Kaplin A, Sevin CM, Brodsky MB, Turnbull AE. Addressing the
1013 post-acute sequelae of SARS-CoV-2 infection: a multidisciplinary model of care. Lancet Respir
1014 Med. 2021;9(11):1328-41. Epub 20211019. doi: 10.1016/S2213-2600(21)00385-4. PubMed
1015 PMID: 34678213; PMCID: PMC8525917.
1016 14. Zhao JM, Zhou GD, Sun YL, Wang SS, Yang JF, Meng EH, Pan D, Li WS, Zhou XS, Wang YD,
1017 Lu JY, Li N, Wang DW, Zhou BC, Zhang TH. [Clinical pathology and pathogenesis of severe acute
1018 respiratory syndrome]. Zhonghua Shi Yan He Lin Chuang Bing Du Xue Za Zhi. 2003;17(3):217-21.
1019 PubMed PMID: 15340561.
1020 15. Xu J, Qi L, Chi X, Yang J, Wei X, Gong E, Peh S, Gu J. Orchitis: a complication of severe
1021 acute respiratory syndrome (SARS). Biol Reprod. 2006;74(2):410-6. Epub 20051019. doi:
1022 10.1095/biolreprod.105.044776. PubMed PMID: 16237152; PMCID: PMC7109827.

1023 16. Beddingfield BJ, Maness NJ, Fears AC, Rappaport J, Aye PP, Russell-Lodrigue K, Doyle-
1024 Meyers LA, Blair RV, Carias AM, Madden PJ, Redondo RL, Gao H, Montefiori D, Hope TJ, Roy CJ.
1025 Effective prophylaxis of COVID-19 in rhesus macaques using a combination of two parentally-
1026 administered SARS-CoV-2 neutralizing antibodies. bioRxiv. 2021:2021.05.26.445878-
1027 2021.05.26. doi: 10.1101/2021.05.26.445878.
1028 17. Blair RV, Vaccari M, Doyle-Meyers LA, Roy CJ, Russell-Lodrigue K, Fahlberg M, Monjure
1029 CJ, Beddingfield B, Plante KS, Plante JA, Weaver SC, Qin X, Midkiff CC, Lehmicke G, Golden N,
1030 Threeton B, Penney T, Allers C, Barnes MB, Pattison M, Datta PK, Maness NJ, Birnbaum A,
1031 Fischer T, Bohm RP, Rappaport J. Acute Respiratory Distress in Aged, SARS-CoV-2–Infected
1032 African Green Monkeys but Not Rhesus Macaques. The American Journal of Pathology.
1033 2021;191(2):274-82. doi: 10.1016/J.AJPATH.2020.10.016.
1034 18. Chandrashekar A, Liu J, Martino AJ, McMahan K, Mercad NB, Peter L, Tostanosk LH, Yu J,
1035 Maliga Z, Nekorchuk M, Busman-Sahay K, Terry M, Wriji LM, Ducat S, Martine DR, Atyeo C,
1036 Fischinger S, Burk JS, Slei MD, Pessaint L, Van Ry A, Greenhouse J, Taylor T, Blade K, Cook A,
1037 Finneyfrock B, Brown R, Teow E, Velasco J, Zahn R, Wegmann F, Abbink P, Bondzi EA, Dagotto
1038 G, Gebr MS, He X, Jacob-Dolan C, Kordana N, Li Z, Lifto MA, Mahrokhia SH, Maxfiel LF,
1039 Nityanandam R, Nkolol JP, Schmid AG, Mille AD, Bari RS, Alter G, Sorge PK, Este JD, Andersen H,
1040 Lewi MG, Barou DH. SARS-CoV-2 infection protects against rechallenge in rhesus macaques.
1041 Science. 2020;369(6505):812-7. doi: 10.1126/SCIENCE.ABC4776.
1042 19. Fahlberg MD, Blair RV, Doyle-Meyers LA, Midkiff CC, Zenere G, Russell-Lodrigue KE,
1043 Monjure CJ, Haupt EH, Penney TP, Lehmicke G, Threeton BM, Golden N, Datta PK, Roy CJ, Bohm
1044 RP, Maness NJ, Fischer T, Rappaport J, Vaccari M. Cellular events of acute, resolving or
1045 progressive COVID-19 in SARS-CoV-2 infected non-human primates. Nat Commun.
1046 2020;11(1):6078. Epub 20201127. doi: 10.1038/s41467-020-19967-4. PubMed PMID:
1047 33247138; PMCID: PMC7695721.
1048 20. Blair RV, Vaccari M, Doyle-Meyers LA, Roy CJ, Russell-Lodrigue K, Fahlberg M, Monjure
1049 CJ, Beddingfield B, Plante KS, Plante JA, Weaver SC, Qin X, Midkiff CC, Lehmicke G, Golden N,
1050 Threeton B, Penney T, Allers C, Barnes MB, Pattison M, Datta PK, Maness NJ, Birnbaum A,
1051 Fischer T, Bohm RP, Rappaport J. Acute Respiratory Distress in Aged, SARS-CoV-2-Infected
1052 African Green Monkeys but Not Rhesus Macaques. Am J Pathol. 2021;191(2):274-82. Epub
1053 20201107. doi: 10.1016/j.ajpath.2020.10.016. PubMed PMID: 33171111; PMCID: PMC7648506.
1054 21. Santangelo PJ, Rogers KA, Zurla C, Blanchard EL, Gumber S, Strait K, Connor-Stroud F,
1055 Schuster DM, Amancha PK, Hong JJ, Byrareddy SN, Hoxie JA, Vidakovic B, Ansari AA, Hunter E,
1056 Villinger F. Whole-body immunoPET reveals active SIV dynamics in viremic and antiretroviral
1057 therapy-treated macaques. Nat Methods. 2015;12(5):427-32. Epub 2015/03/10. doi:
1058 10.1038/nmeth.3320. PubMed PMID: 25751144; PMCID: PMC4425449.
1059 22. Taylor RA, McRaven MD, Carias AM, Anderson MR, Matias E, Arainga M, Allen EJ, Rogers
1060 KA, Gupta S, Kulkarni V, Lakhashe S, Lorenzo-Redondo R, Thomas Y, Strickland A, Villinger FJ,
1061 Ruprecht RM, Hope TJ. Localization of infection in neonatal rhesus macaques after oral viral
1062 challenge. PLoS Pathog. 2021;17(11):e1009855. Epub 20211118. doi:
1063 10.1371/journal.ppat.1009855. PubMed PMID: 34793582; PMCID: PMC8639050.
1064 23. Taylor RA, Xiao S, Carias AM, McRaven MD, Thakkar DN, Arainga M, Allen EJ, Rogers KA,
1065 Kumarapperuma SC, Gong S, Fought AJ, Anderson MR, Thomas Y, Schneider JR, Goins B, Fox P,
1066 Villinger FJ, Ruprecht RM, Hope TJ. PET/CT targeted tissue sampling reveals virus specific dIgA

1067 can alter the distribution and localization of HIV after rectal exposure. PLoS Pathog.
1068 2021;17(6):e1009632. Epub 20210601. doi: 10.1371/journal.ppat.1009632. PubMed PMID:
1069 34061907; PMCID: PMC8195437.
1070 24. Madden PJ, Arif MS, Becker ME, McRaven MD, Carias AM, Lorenzo-Redondo R, Xiao S,
1071 Midkiff CC, Blair RV, Potter EL, Martin-Sancho L, Dodson A, Martinelli E, Todd JM, Villinger FJ,
1072 Chanda SK, Aye PP, Roy CJ, Roederer M, Lewis MG, Veazey RS, Hope TJ. Development of an In
1073 Vivo Probe to Track SARS-CoV-2 Infection in Rhesus Macaques. Front Immunol.
1074 2021;12:810047. Epub 20211224. doi: 10.3389/fimmu.2021.810047. PubMed PMID: 35003140;
1075 PMCID: PMC8739270.
1076 25. Fahlberg MD, Blair RV, Doyle-Meyers LA, Midkiff CC, Zenere G, Russell-Lodrigue KE,
1077 Monjure CJ, Haupt EH, Penney TP, Lehmicke G, Threeton BM, Golden N, Datta PK, Roy CJ, Bohm
1078 RP, Maness NJ, Fischer T, Rappaport J, Vaccari M. Cellular events of acute, resolving or
1079 progressive COVID-19 in SARS-CoV-2 infected non-human primates. Nature Communications
1080 2020 11:1. 2020;11(1):1-14. doi: 10.1038/s41467-020-19967-4.
1081 26. Gao G, Hu X, Zhou Y, Rao J, Zhang X, Peng Y, Zhao J, Yao Y, Liu K, Liang M, Liu H, Deng F,
1082 Xia H, Shan C, Yuan Z. Infection and pathogenesis of the Delta variant of SARS-CoV-2 in Rhesus
1083 macaque. Virologica Sinica. 2022. doi: 10.1016/j.virs.2022.02.001.
1084 27. Nicolas N, Michel V, Bhushan S, Wahle E, Hayward S, Ludlow H, de Kretser DM, Loveland
1085 KL, Schuppe HC, Meinhardt A, Hedger MP, Fijak M. Testicular activin and follistatin levels are
1086 elevated during the course of experimental autoimmune epididymo-orchitis in mice. Sci Rep.
1087 2017;7:42391. Epub 20170213. doi: 10.1038/srep42391. PubMed PMID: 28205525; PMCID:
1088 PMC5304336.
1089 28. Cardona-Maya W, Velilla PA, Montoya CJ, Cadavid A, Rugeles MT. In vitro human
1090 immunodeficiency virus and sperm cell interaction mediated by the mannose receptor. J
1091 Reprod Immunol. 2011;92(1-2):1-7. Epub 20111019. doi: 10.1016/j.jri.2011.09.002. PubMed
1092 PMID: 22015004.
1093 29. Cardona-Maya W, Lopez-Herrera A, Velilla-Hernandez P, Rugeles MT, Cadavid AP. The
1094 role of mannose receptor on HIV-1 entry into human spermatozoa. Am J Reprod Immunol.
1095 2006;55(4):241-5. doi: 10.1111/j.1600-0897.2005.00340.x. PubMed PMID: 16533334.
1096 30. Benoff S, Hurley I, Cooper GW, Mandel FS, Hershlag A, Scholl GM, Rosenfeld DL.
1097 Fertilization potential in vitro is correlated with head-specific mannose-ligand receptor
1098 expression, acrosome status and membrane cholesterol content. Hum Reprod.
1099 1993;8(12):2155-66. doi: 10.1093/oxfordjournals.humrep.a137997. PubMed PMID: 8150918.
1100 31. Corbett KS, Flynn B, Foulds KE, Francica JR, Boyoglu-Barnum S, Werner AP, Flach B,
1101 O'Connell S, Bock KW, Minai M, Nagata BM, Andersen H, Martinez DR, Noe AT, Douek N,
1102 Donaldson MM, Nji NN, Alvarado GS, Edwards DK, Flebbe DR, Lamb E, Doria-Rose NA, Lin BC,
1103 Louder MK, O'Dell S, Schmidt SD, Phung E, Chang LA, Yap C, Todd J-PM, Pessaint L, Ry AV,
1104 Browne S, Greenhouse J, Putman-Taylor T, Strasbaugh A, Campbell T-A, Cook A, Dodson A,
1105 Steingrebe K, Shi W, Zhang Y, Abiona OM, Wang L, Pegu A, Yang ES, Leung K, Zhou T, Teng IT,
1106 Widge A, Gordon I, Novik L, Gillespie RA, Loomis RJ, Moliva JI, Stewart-Jones G, Himansu S, Kong
1107 W-P, Nason MC, Morabito KM, Ruckwardt TJ, Ledgerwood JE, Gaudinski MR, Kwong PD,
1108 Mascola JR, Carfi A, Lewis MG, Baric RS, McDermott A, Moore IN, Sullivan NJ, Roederer M,
1109 Seder RA, Graham BS. Evaluation of the mRNA-1273 Vaccine against SARS-CoV-2 in Nonhuman

1110 Primates. https://doiorg/101056/NEJMoa2024671. 2020;383(16):1544-55. doi:
1111 10.1056/NEJMOA2024671.
1112 32. Lindsay KE, Bhosle SM, Zurla C, Beyersdorf J, Rogers KA, Vanover D, Xiao P, Araínga M,
1113 Shirreff LM, Pitard B, Baumhof P, Villinger F, Santangelo PJ. Visualization of early events in
1114 mRNA vaccine delivery in non-human primates via PET–CT and near-infrared imaging. Nature
1115 Biomedical Engineering 2019 3:5. 2019;3(5):371-80. doi: 10.1038/s41551-019-0378-3.
1116 33. Soriano JB, Murthy S, Marshall JC, Relan P, Diaz JV, Condition WHOCCDWGoP-C-. A
1117 clinical case definition of post-COVID-19 condition by a Delphi consensus. Lancet Infect Dis.
1118 2021. Epub 20211221. doi: 10.1016/S1473-3099(21)00703-9. PubMed PMID: 34951953;
1119 PMCID: PMC8691845.
1120 34. Ward H, Flower B, Garcia PJ, Ong SWX, Altmann DM, Delaney B, Smith N, Elliott P, Cooke
1121 G. Global surveillance, research, and collaboration needed to improve understanding and
1122 management of long COVID. Lancet. 2021;398(10316):2057-9. Epub 20211110. doi:
1123 10.1016/S0140-6736(21)02444-2. PubMed PMID: 34774190; PMCID: PMC8580495.
1124 35. Duarte-Neto AN, Teixeira TA, Caldini EG, Kanamura CT, Gomes-Gouvea MS, Dos Santos
1125 ABG, Monteiro RAA, Pinho JRR, Mauad T, da Silva LFF, Saldiva PHN, Dolhnikoff M, Leite KRM,
1126 Hallak J. Testicular pathology in fatal COVID-19: A descriptive autopsy study. Andrology.
1127 2022;10(1):13-23. Epub 20210716. doi: 10.1111/andr.13073. PubMed PMID: 34196475; PMCID:
1128 PMC8444746.
1129 36. Moghimi N, Eslami Farsani B, Ghadipasha M, Mahmoudiasl GR, Piryaei A, Aliaghaei A,
1130 Abdi S, Abbaszadeh HA, Abdollahifar MA, Forozesh M. COVID-19 disrupts spermatogenesis
1131 through the oxidative stress pathway following induction of apoptosis. Apoptosis. 2021;26(7-
1132 8):415-30. Epub 20210602. doi: 10.1007/s10495-021-01680-2. PubMed PMID: 34076792;
1133 PMCID: PMC8170653.
1134 37. Yang M, Chen S, Huang B, Zhong JM, Su H, Chen YJ, Cao Q, Ma L, He J, Li XF, Li X, Zhou JJ,
1135 Fan J, Luo DJ, Chang XN, Arkun K, Zhou M, Nie X. Pathological Findings in the Testes of COVID-
1136 19 Patients: Clinical Implications. Eur Urol Focus. 2020;6(5):1124-9. Epub 20200531. doi:
1137 10.1016/j.euf.2020.05.009. PubMed PMID: 32563676; PMCID: PMC7261470.
1138 38. Peirouvi T, Aliaghaei A, Eslami Farsani B, Ziaeipour S, Ebrahimi V, Forozesh M,
1139 Ghadipasha M, Mahmoudiasl GR, Aryan A, Moghimi N, Abdi S, Raoofi A, Kargar Godaneh M,
1140 Abdollahifar MA. COVID-19 disrupts the blood-testis barrier through the induction of
1141 inflammatory cytokines and disruption of junctional proteins. Inflamm Res. 2021;70(10-
1142 12):1165-75. Epub 20210826. doi: 10.1007/s00011-021-01497-4. PubMed PMID: 34436630;
1143 PMCID: PMC8387554.
1144 39. Achua JK, Chu KY, Ibrahim E, Khodamoradi K, Delma KS, Iakymenko OA, Kryvenko ON,
1145 Arora H, Ramasamy R. Histopathology and Ultrastructural Findings of Fatal COVID-19 Infections
1146 on Testis. World J Mens Health. 2021;39(1):65-74. Epub 20201103. doi: 10.5534/wjmh.200170.
1147 PubMed PMID: 33151050; PMCID: PMC7752514.
1148 40. Ma X, Guan C, Chen R, Wang Y, Feng S, Wang R, Qu G, Zhao S, Wang F, Wang X, Zhang D,
1149 Liu L, Liao A, Yuan S. Pathological and molecular examinations of postmortem testis biopsies
1150 reveal SARS-CoV-2 infection in the testis and spermatogenesis damage in COVID-19 patients.
1151 Cellular and Molecular Immunology. 2021;18(2):487-9. doi: 10.1038/s41423-020-00604-5.

1152 41. Ardestani Zadeh A, Arab D. COVID-19 and male reproductive system: pathogenic
1153 features and possible mechanisms. J Mol Histol. 2021;52(5):869-78. Epub 20210707. doi:
1154 10.1007/s10735-021-10003-3. PubMed PMID: 34232425; PMCID: PMC8260577.
1155 42. Liu X, Chen Y, Tang W, Zhang L, Chen W, Yan Z, Yuan P, Yang M, Kong S, Yan L, Qiao J.
1156 Single-cell transcriptome analysis of the novel coronavirus (SARS-CoV-2) associated gene ACE2
1157 expression in normal and non-obstructive azoospermia (NOA) human male testes. Sci China Life
1158 Sci. 2020;63(7):1006-15. Epub 20200430. doi: 10.1007/s11427-020-1705-0. PubMed PMID:
1159 32361911; PMCID: PMC7195615.
1160 43. Li X, Lu H, Li F, Zhang Q, Wang T, Qiang L, Yang Q. Impacts of COVID-19 and SARS-CoV-2
1161 on male reproductive function: a systematic review and meta-analysis protocol. BMJ Open.
1162 2022;12(1):e053051. Epub 20220105. doi: 10.1136/bmjopen-2021-053051. PubMed PMID:
1163 34987042.
1164 44. Li C, Ye Z, Zhang AJ, Chan JF, Song W, Liu F, Chen Y, Kwan MY, Lee AC, Zhao Y, Wong BH,
1165 Yip CC, Cai JP, Lung DC, Sridhar S, Jin D, Chu H, To KK, Yuen KY. Severe acute respiratory
1166 syndrome coronavirus 2 (SARS-CoV-2) infections by intranasal or testicular inoculation induces
1167 testicular damage preventable by vaccination in golden Syrian hamsters. Clin Infect Dis. 2022.
1168 Epub 20220218. doi: 10.1093/cid/ciac142. PubMed PMID: 35178548.
1169 45. Campos RK, Camargos VN, Azar SR, Haines CA, Eyzaguirre EJ, Rossi SL. SARS-CoV-2
1170 Infects Hamster Testes. Microorganisms. 2021;9(6). Epub 20210617. doi:
1171 10.3390/microorganisms9061318. PubMed PMID: 34204370; PMCID: PMC8235703.
1172 46. Ullah I, Prevost J, Ladinsky MS, Stone H, Lu M, Anand SP, Beaudoin-Bussieres G, Symmes
1173 K, Benlarbi M, Ding S, Gasser R, Fink C, Chen Y, Tauzin A, Goyette G, Bourassa C, Medjahed H,
1174 Mack M, Chung K, Wilen CB, Dekaban GA, Dikeakos JD, Bruce EA, Kaufmann DE, Stamatatos L,
1175 McGuire AT, Richard J, Pazgier M, Bjorkman PJ, Mothes W, Finzi A, Kumar P, Uchil PD. Live
1176 imaging of SARS-CoV-2 infection in mice reveals that neutralizing antibodies require Fc function
1177 for optimal efficacy. Immunity. 2021;54(9):2143-58 e15. Epub 20210818. doi:
1178 10.1016/j.immuni.2021.08.015. PubMed PMID: 34453881; PMCID: PMC8372518.
1179 47. Pike JFW, Polley EL, Pritchett DY, Lal A, Wynia BA, Roudebush WE, Chosed RJ.
1180 Comparative analysis of viral infection outcomes in human seminal fluid from prior viral
1181 epidemics and Sars-CoV-2 may offer trends for viral sexual transmissibility and long-term
1182 reproductive health implications. Reprod Health. 2021;18(1):123. Epub 20210610. doi:
1183 10.1186/s12978-021-01172-1. PubMed PMID: 34112171; PMCID: PMC8192109.
1184 48. Massarotti C, Garolla A, Maccarini E, Scaruffi P, Stigliani S, Anserini P, Foresta C. SARS-
1185 CoV-2 in the semen: Where does it come from? Andrology. 2021;9(1):39-41. Epub 20200728.
1186 doi: 10.1111/andr.12839. PubMed PMID: 32533891; PMCID: PMC7323151.
1187 49. Haghpanah A, Masjedi F, Salehipour M, Hosseinpour A, Roozbeh J, Dehghani A. Is
1188 COVID-19 a risk factor for progression of benign prostatic hyperplasia and exacerbation of its
1189 related symptoms?: a systematic review. Prostate Cancer Prostatic Dis. 2021. Epub 20210518.
1190 doi: 10.1038/s41391-021-00388-3. PubMed PMID: 34007019; PMCID: PMC8129694.
1191 50. Stopsack KH, Mucci LA, Antonarakis ES, Nelson PS, Kantoff PW. TMPRSS2 and COVID-19:
1192 Serendipity or Opportunity for Intervention? Cancer Discov. 2020;10(6):779-82. Epub
1193 20200410. doi: 10.1158/2159-8290.CD-20-0451. PubMed PMID: 32276929; PMCID:
1194 PMC7437472.

1195 51. Gedeborg R, Styrke J, Loeb S, Garmo H, Stattin P. Androgen deprivation therapy and
1196 excess mortality in men with prostate cancer during the initial phase of the COVID-19
1197 pandemic. PLoS One. 2021;16(10):e0255966. Epub 20211007. doi:
1198 10.1371/journal.pone.0255966. PubMed PMID: 34618806; PMCID: PMC8496782.
1199 52. Soumarova R, Boday A, Krhutova V, Janotova A, Dvorakova M, Jaluvkova E, Stursa M,
1200 Perkova H. Prognostic and predictive molecular biological markers in prostate cancer -
1201 significance of expression of genes PCA3 and TMPRSS2. Neoplasma. 2015;62(1):114-8. doi:
1202 10.4149/neo_2015_014. PubMed PMID: 25563374.
1203 53. Bhowmick NA, Oft J, Dorff T, Pal S, Agarwal N, Figlin RA, Posadas EM, Freedland SJ, Gong
1204 J. COVID-19 and androgen-targeted therapy for prostate cancer patients. Endocr Relat Cancer.
1205 2020;27(9):R281-R92. doi: 10.1530/ERC-20-0165. PubMed PMID: 32508311; PMCID:
1206 PMC7546583.
1207 54. Kazan O, Culpan M, Efiloglu O, Atis G, Yildirim A. The clinical impact of androgen
1208 deprivation therapy on SARS-CoV-2 infection rates and disease severity. Turk J Urol.
1209 2021;47(6):495-500. doi: 10.5152/tud.2021.21278. PubMed PMID: 35118968.
1210 55. Cinislioglu AE, Demirdogen SO, Cinislioglu N, Altay MS, Sam E, Akkas F, Tor IH, Aydin HR,
1211 Karabulut I, Ozbey I. Variation of Serum PSA Levels in COVID-19 Infected Male Patients with
1212 Benign Prostatic Hyperplasia (BPH): A Prospective Cohort Studys. Urology. 2022;159:16-21.
1213 Epub 20211006. doi: 10.1016/j.urology.2021.09.016. PubMed PMID: 34626600; PMCID:
1214 PMC8493783.
1215 56. Mohamed MS, Moulin TC, Schioth HB. Sex differences in COVID-19: the role of
1216 androgens in disease severity and progression. Endocrine. 2021;71(1):3-8. Epub 20201111. doi:
1217 10.1007/s12020-020-02536-6. PubMed PMID: 33179220; PMCID: PMC7657570.
1218 57. Reddy R, Farber N, Kresch E, Seetharam D, Diaz P, Ramasamy R. SARS-CoV-2 in the
1219 Prostate: Immunohistochemical and Ultrastructural Studies. The World Journal of Men's Health.
1220 2021;40. doi: 10.5534/WJMH.210174.
1221 58. Fraga-Silva RA, Costa-Fraga FP, Montecucco F, Sturny M, Faye Y, Mach F, Pelli G, Shenoy
1222 V, da Silva RF, Raizada MK, Santos RA, Stergiopulos N. Diminazene protects corpus cavernosum
1223 against hypercholesterolemia-induced injury. J Sex Med. 2015;12(2):289-302. Epub 20141120.
1224 doi: 10.1111/jsm.12757. PubMed PMID: 25411084.
1225 59. Kresch E, Achua J, Saltzman R, Khodamoradi K, Arora H, Ibrahim E, Kryvenko ON, Wolff
1226 Almeida V, Firdaus F, Hare JM, Ramasamy R. COVID-19 Endothelial Dysfunction Can Cause
1227 Erectile Dysfunction: Histopathological, Immunohistochemical, and Ultrastructural Study of the
1228 Human Penis. World J Mens Health. 2021;39:2287-4208. doi: 10.5534/wjmh.210055.
1229 60. Sansone A, Mollaioli D, Ciocca G, Colonnello E, Limoncin E, Balercia G, Jannini EA. “Mask
1230 up to keep it up”: Preliminary evidence of the association between erectile dysfunction and
1231 COVID-19. Andrology. 2021;00:1-7. doi: 10.1111/andr.13003.
1232 61. Dal Moro F, Vendramin I, Livi U. The war against the SARS-CoV2 infection: Is it better to
1233 fight or mitigate it? Med Hypotheses. 2020;143:110129. Epub 20200722. doi:
1234 10.1016/j.mehy.2020.110129. PubMed PMID: 32721814; PMCID: PMC7373683.
1235 62. Mejri R, Mrad Dali K, Chaker K, Bibi M, Ben Rhouma S, Nouira Y. Venous thrombosis of
1236 the pampiniform plexus after coronavirus infection (COVID-19): A case report. Urol Case Rep.
1237 2021;39:101860. Epub 20210927. doi: 10.1016/j.eucr.2021.101860. PubMed PMID: 34603969;
1238 PMCID: PMC8475016.

1239 63. Alshoabi SA, Haider KH, Mostafa MA, Hamid AM, Daqqaq TS. An unusual and atypical
1240 presentation of the novel coronavirus: A case report and brief review of the literature. J Taibah
1241 Univ Med Sci. 2021;16(4):637-42. Epub 20210412. doi: 10.1016/j.jtumed.2021.01.014. PubMed
1242 PMID: 33867909; PMCID: PMC8038890.
1243 64. Whiteley MS, Abu-Bakr O, Holdstock JM. Testicular vein thrombosis mimicking
1244 epididymo-orchitis after suspected Covid-19 infection. SAGE Open Med Case Rep.
1245 2021;9:2050313X211022425. Epub 20210604. doi: 10.1177/2050313X211022425. PubMed
1246 PMID: 34158948; PMCID: PMC8182169.
1247 65. La Marca A, Busani S, Donno V, Guaraldi G, Ligabue G, Girardis M. Testicular pain as an
1248 unusual presentation of COVID-19: a brief review of SARS-CoV-2 and the testis. Reprod Biomed
1249 Online. 2020;41(5):903-6. Epub 20200723. doi: 10.1016/j.rbmo.2020.07.017. PubMed PMID:
1250 32826162; PMCID: PMC7377719.
1251 66. Li K, Liu X, Huang Y, Liu X, Song Q, Wang R. Evaluation of testicular spermatogenic
1252 function by ultrasound elastography in patients with varicocele-associated infertility. Am J
1253 Transl Res. 2021;13(8):9136-42. Epub 20210815. PubMed PMID: 34540028; PMCID:
1254 PMC8430184.
1255 67. Mali WP, Arndt JW, Coolsaet BL, Kremer J, Oei HY. Haemodynamic aspects of left-sided
1256 varicocele and its association with so-called right-sided varicocele. Int J Androl. 1984;7(4):297-
1257 308. doi: 10.1111/j.1365-2605.1984.tb00787.x. PubMed PMID: 6096276.
1258 68. Aitken RJ. COVID-19 and human spermatozoa—Potential risks for infertility and sexual
1259 transmission? Andrology. 2021;9(1):48-52. doi: 10.1111/andr.12859.
1260 69. Gacci M, Coppi M, Baldi E, Sebastianelli A, Zaccaro C, Morselli S, Pecoraro A, Manera A,
1261 Nicoletti R, Liaci A, Bisegna C, Gemma L, Giancane S, Pollini S, Antonelli A, Lagi F, Marchiani S,
1262 Dabizzi S, Degl'Innocenti S, Annunziato F, Maggi M, Vignozzi L, Bartoloni A, Rossolini GM, Serni
1263 S. Semen impairment and occurrence of SARS-CoV-2 virus in semen after recovery from COVID-
1264 19. Human Reproduction. 2021;0(0):1-10. doi: 10.1093/humrep/deab026.
1265 70. Sengupta P, Leisegang K, Agarwal A. The impact of COVID-19 on the male reproductive
1266 tract and fertility: A systematic review. Arab J Urol. 2021;19(3):423-36. Epub 20210809. doi:
1267 10.1080/2090598X.2021.1955554. PubMed PMID: 34552795; PMCID: PMC8451696.
1268 71. Li H, Xiao X, Zhang J, Zafar MI, Wu C, Long Y, Lu W, Pan F, Meng T, Zhao K, Zhou L, Shen
1269 S, Liu L, Liu Q, Xiong C. Impaired spermatogenesis in COVID-19 patients. EClinicalMedicine.
1270 2020;28. doi: 10.1016/j.eclinm.2020.100604.
1271 72. Delli Muti N, Finocchi F, Tossetta G, Salvio G, Cutini M, Marzioni D, Balercia G. Could
1272 SARS-CoV-2 infection affect male fertility and sexuality? APMIS. 2022. Epub 20220203. doi:
1273 10.1111/apm.13210. PubMed PMID: 35114008.
1274 73. Wesselink AK, Hatch EE, Rothman KJ, Wang TR, Willis MD, Yland J, Crowe HM, Geller RJ,
1275 Willis SK, Perkins RB, Regan AK, Levinson J, Mikkelsen EM, Wise LA. A prospective cohort study
1276 of COVID-19 vaccination, SARS-CoV-2 infection, and fertility. Am J Epidemiol. 2022. Epub
1277 20220120. doi: 10.1093/aje/kwac011. PubMed PMID: 35051292; PMCID: PMC8807200.
1278 74. Xu J, Qi L, Chi X, Yang J, Wei X, Gong E, Peh S, Gu J. Orchitis: A Complication of Severe
1279 Acute Respiratory Syndrome (SARS). Biology of Reproduction. 2006;74(2):410-6. doi:
1280 10.1095/BIOLREPROD.105.044776.

1281 75. Delle Fave RF, Polisini G, Giglioni G, Parlavecchio A, Dell'Atti L, Galosi AB. COVID-19 and
1282 male fertility: Taking stock of one year after the outbreak began. Archivio Italiano di Urologia e
1283 Andrologia. 2021;93(1):115-9. doi: 10.4081/aiua.2021.1.115.
1284 76. Al-Kuraishy HM, Al-Gareeb AI, Faidah H, Alexiou A, Batiha GE. Testosterone in COVID-19:
1285 An Adversary Bane or Comrade Boon. Front Cell Infect Microbiol. 2021;11:666987. Epub
1286 20210908. doi: 10.3389/fcimb.2021.666987. PubMed PMID: 34568081; PMCID: PMC8455954.
1287 77. Haghpanah A, Masjedi F, Alborzi S, Hosseinpour A, Dehghani A, Malekmakan L, Roozbeh
1288 J. Potential mechanisms of SARS-CoV-2 action on male gonadal function and fertility: Current
1289 status and future prospects. Andrologia. 2021;53(1):e13883-e. doi: 10.1111/and.13883.
1290 78. Enikeev D, Taratkin M, Morozov A, Petov V, Korolev D, Shpikina A, Spivak L, Kharlamova
1291 S, Shchedrina I, Mestnikov O, Fiev D, Ganzha T, Geladze M, Mambetova A, Kogan E, Zharkov N,
1292 Demyashkin G, Shariat SF, Glybochko P. Prospective two-arm study of the testicular function in
1293 patients with COVID-19. Andrology. 2022. Epub 20220206. doi: 10.1111/andr.13159. PubMed
1294 PMID: 35124885.
1295

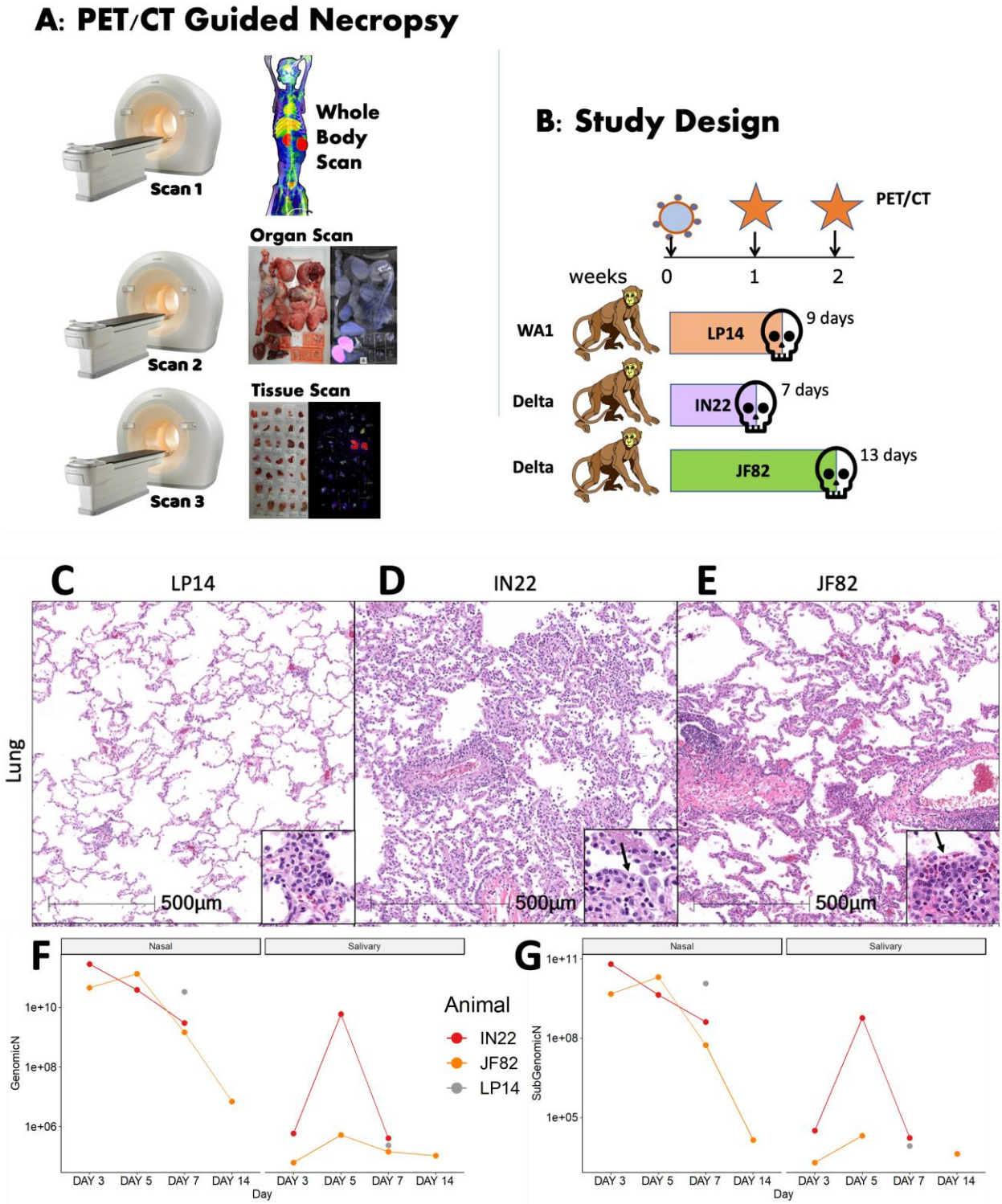

Figure 1. Study design and viral analysis of infected macaques. (A) Workflow of PET/CT guided necropsy. (B) Schematic showing the study design of probe administration, PET/CT scans, and infection. (C-E) Lung lesions were consistent with prior findings in NHPs infected with SARS-CoV-2 and varied from minimal in LP14 (C), moderate in IN22 (D), and mild in JF82 (E). Insets demonstrate the inflammatory infiltrate and in IN22 and JF82, type II pneumocyte hyperplasia (arrows). (F and G) Viral load measurements for all three animals. (F) shows copies/swab of genomic N while (G) shows copies/swab of subgenomic N.

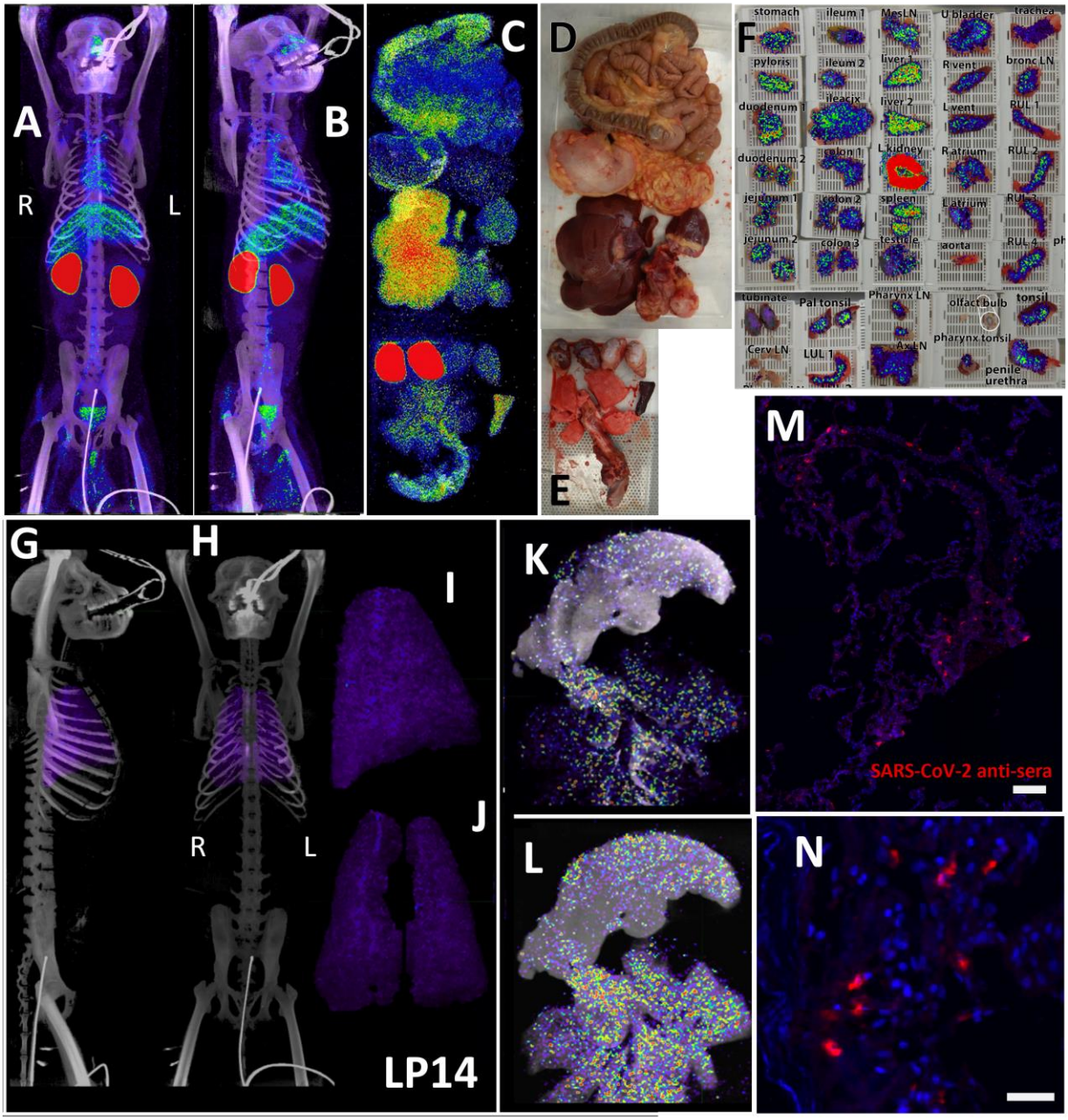

Figure 2. LP14 PET/CT guided necropsy. (A and B) Whole-body PET/CT scans of LP14 8 days post-infection. Front view (A) and rotated 45° (B) both shown. PET signal is display as SUV. (C) Post necropsy PET/CT organ scan of LP14. (D and E) Images of tissues scanned in (C). (F) Overlay of PET signal onto photograph of small pieces of tissue in cassettes. (G and H) Lung PET signal was isolated and overlaid on whole body CT scans. Side (G) and front (H) view. (I and J) Isolated lung PET volumes used in G and H are shown independently, side view (I) and front view (J). (K and L) Single axial z-slice images of respiratory tract PET/CT signals are shown, each image represents a single z-plane from scan shown in C. (M and N) Fluorescent microscopy images of LP14 lung tissue blocks. Red is SARS-CoV-2 anti-sera and blue is Hoechst nuclear stain. Scale bars 100 µM (M) and 25 µM (N).

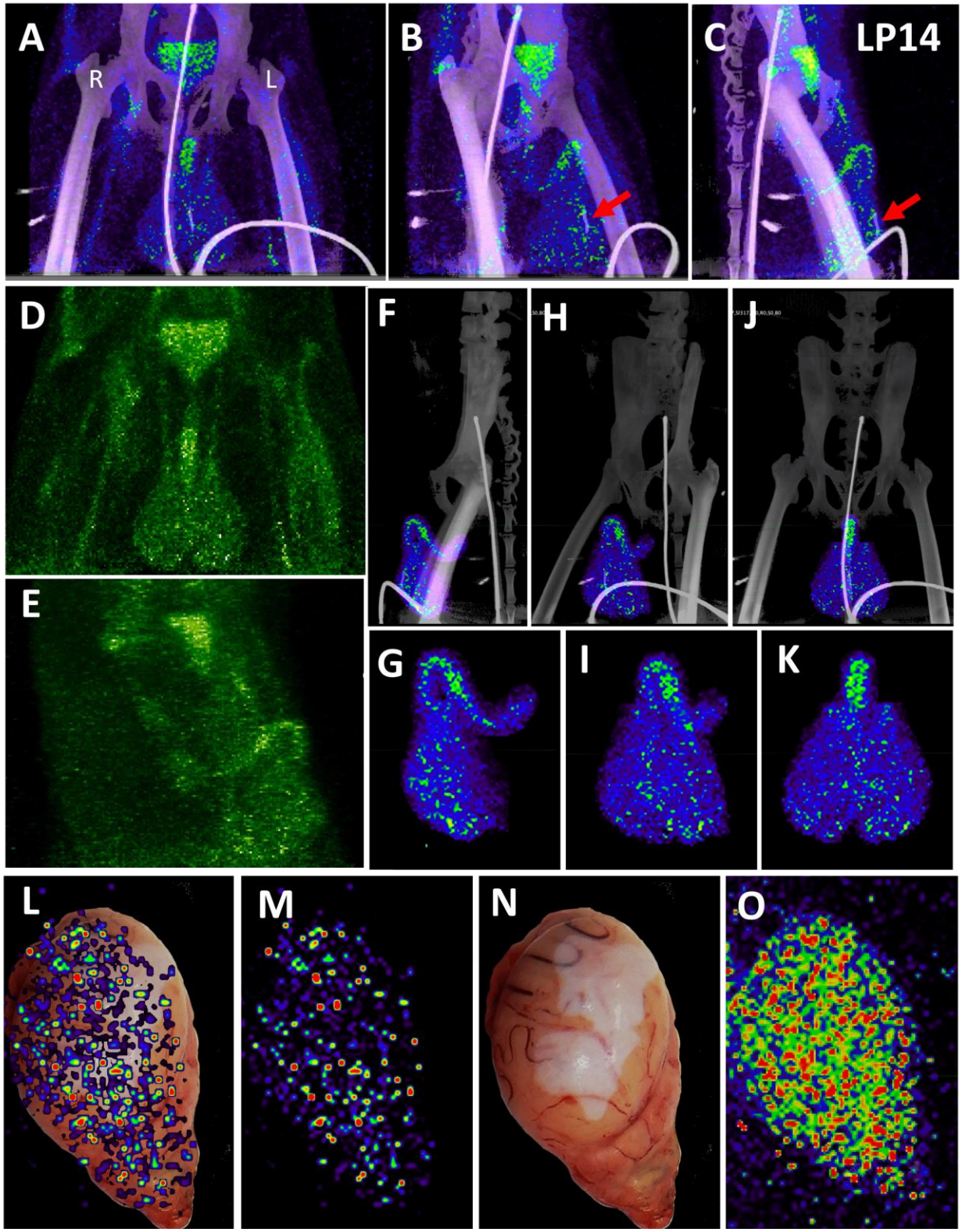

1176
1177
1178

1179 **Figure 3. Male genital tract signal in LP14.** (A, B, and C) PET/CT images highlighting the lower
1180 abdomen of LP14 from the whole-body scan. Front (A), rotated 45° (B), and side (C) views are
1181 all shown. Right and left labeled in front view. Red arrow in B and C shows location of baculum
1182 in CT scan. (D and E) PET signal with CT overlay removed to highlight signal in MGT, front (D)
1183 and side (E) views shown. (F, H, and J) Isolated 3D volume of MGT from whole body scan
1184 overlaid with CT images. Side (F), rotated 45° (H), and front (J) views shown. (G, I, and K)
1185 Isolated 3D volume of MGT used in overlays (F, H, and J) shown with same views. (L) Overlay of
1186 single z-plane of PET signal from organ scan onto image of testis of LP14. (M) PET signal from
1187 single z-plane of organ scan used in (L). (N) Image of LP14 testis used in (L). (O) 3D volume of
1188 PET signal from organ scan of single testis in previous panels.
1189

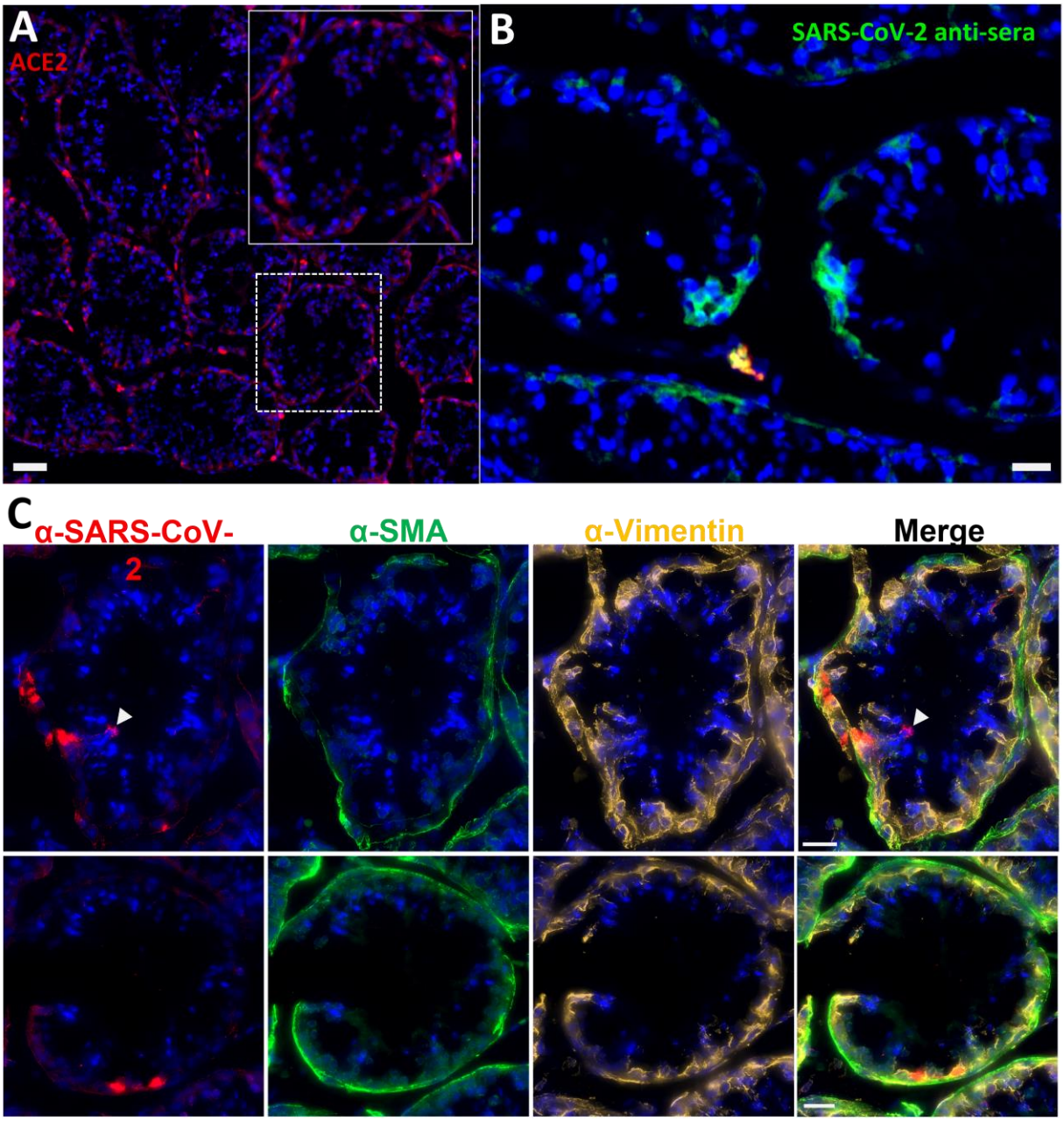

Figure 4. Immunofluorescence of LP14 Testes. (A) Fluorescent microscopy image of LP14 seminiferous tubules. ACE2 staining shown in red, Hoechst nuclear staining shown in blue. Inset shows zoom in of single tubule to better view ACE2 staining in Sertoli and myoid cells. Scale bars 50 µM. (B) Fluorescent microscopy image of LP14 testis shows infected cells. SARS-CoV-2 anti-sera staining in green, background fluorescent in red, and Hoechst nuclear staining in blue. Scale bars 25 µM. (C) Microscopy images of two tubules containing infected cells (top and bottom rows). Red is SARS-CoV-2 anti-sera, green is smooth muscle actin, gold is vimentin, and blue is Hoechst nuclear stain. Possible infected germ cells marked by arrow heads. Scale bars 20 µM.

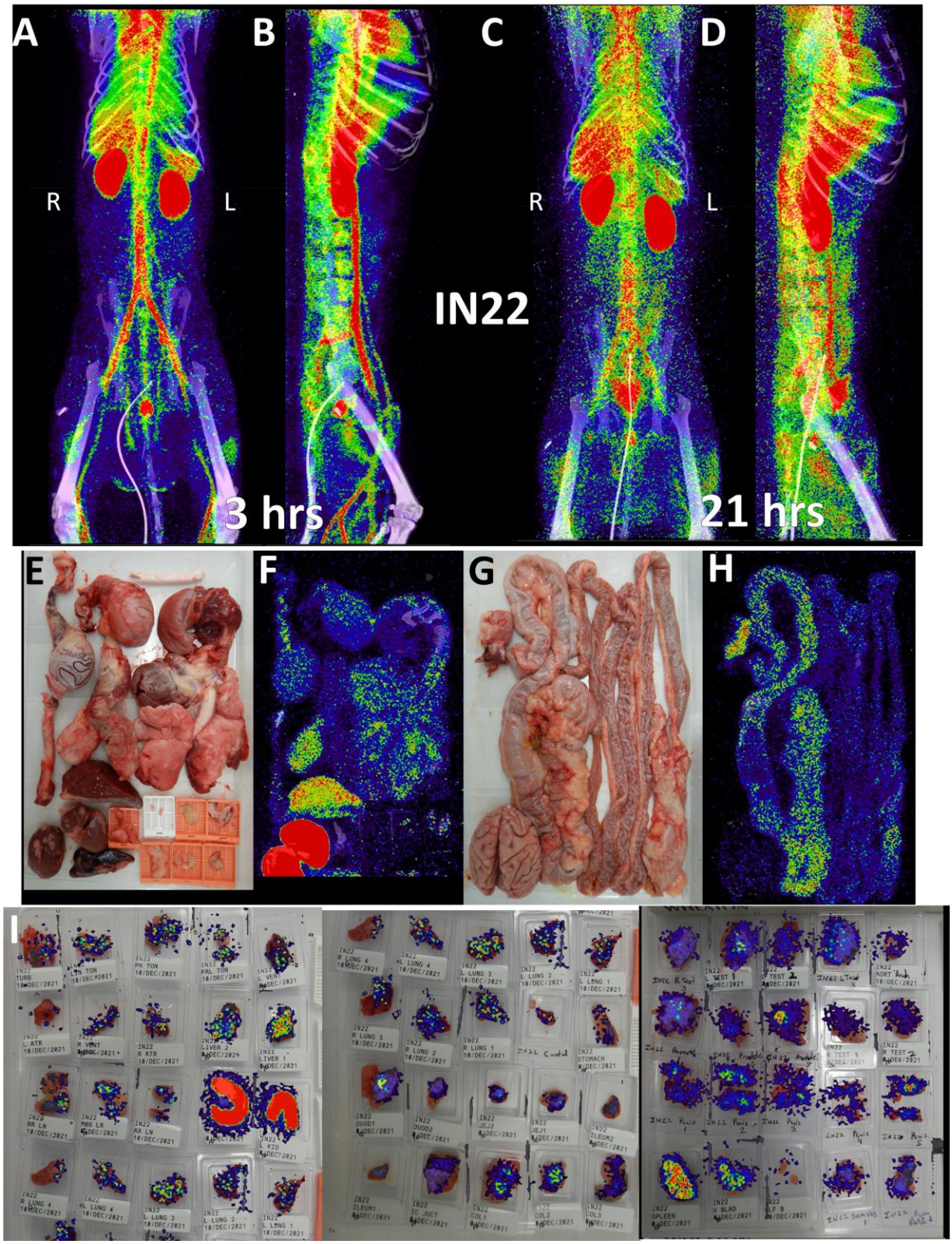
A
B
C
D
R
L
R
L
IN22
3 hrs
21 hrs
E
F
G
H
I

1205 **Figure 5. IN22 PET/CT guided necropsy images.** (A and B) Whole-body PET/CT scans of IN22
1206 obtained 3-hours after probe administration. Front view (A) and side (B) both shown. (C and D)
1207 Whole-body PET/CT scans of IN22 obtained 21-hours after probe administration. Front view (C)
1208 and side (D) both shown. Right and left labeled in front views (A and C). (E) Organ tray post
1209 necropsy and (F) PET/CT image. (G) Second organ tray post necropsy and (H) PET/CT image. (I)
1210 Overlay of PET signal onto photograph of tissue cassettes.
1211

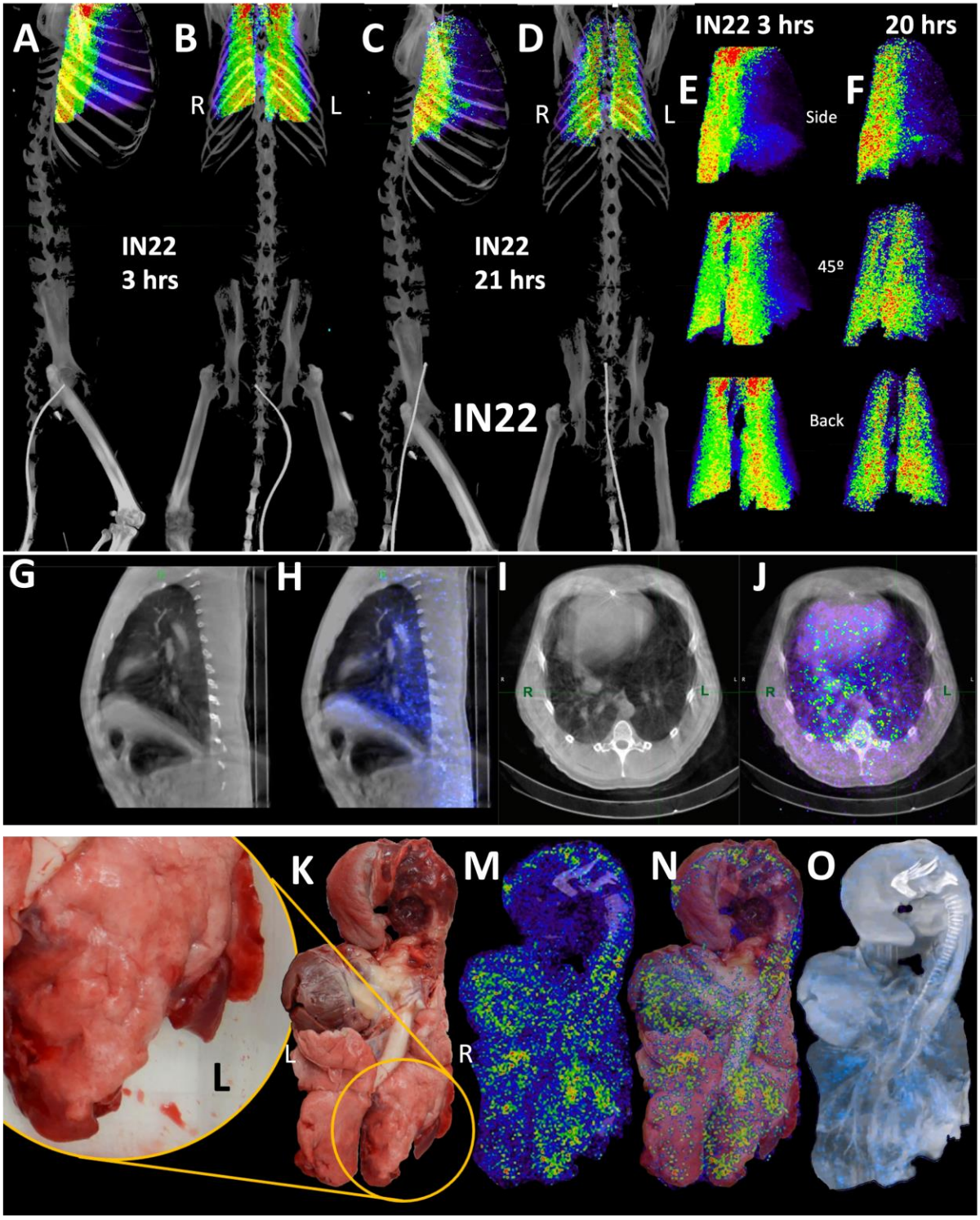
A
B
C
D
R
L
R
L
IN22 3 hrs
20 hrs
E
F
Side
IN22
3 hrs
IN22
21 hrs
45º
IN22
Back
G
H
I
J
R
L
R
L
K
M
N
O
L
L
R

1212

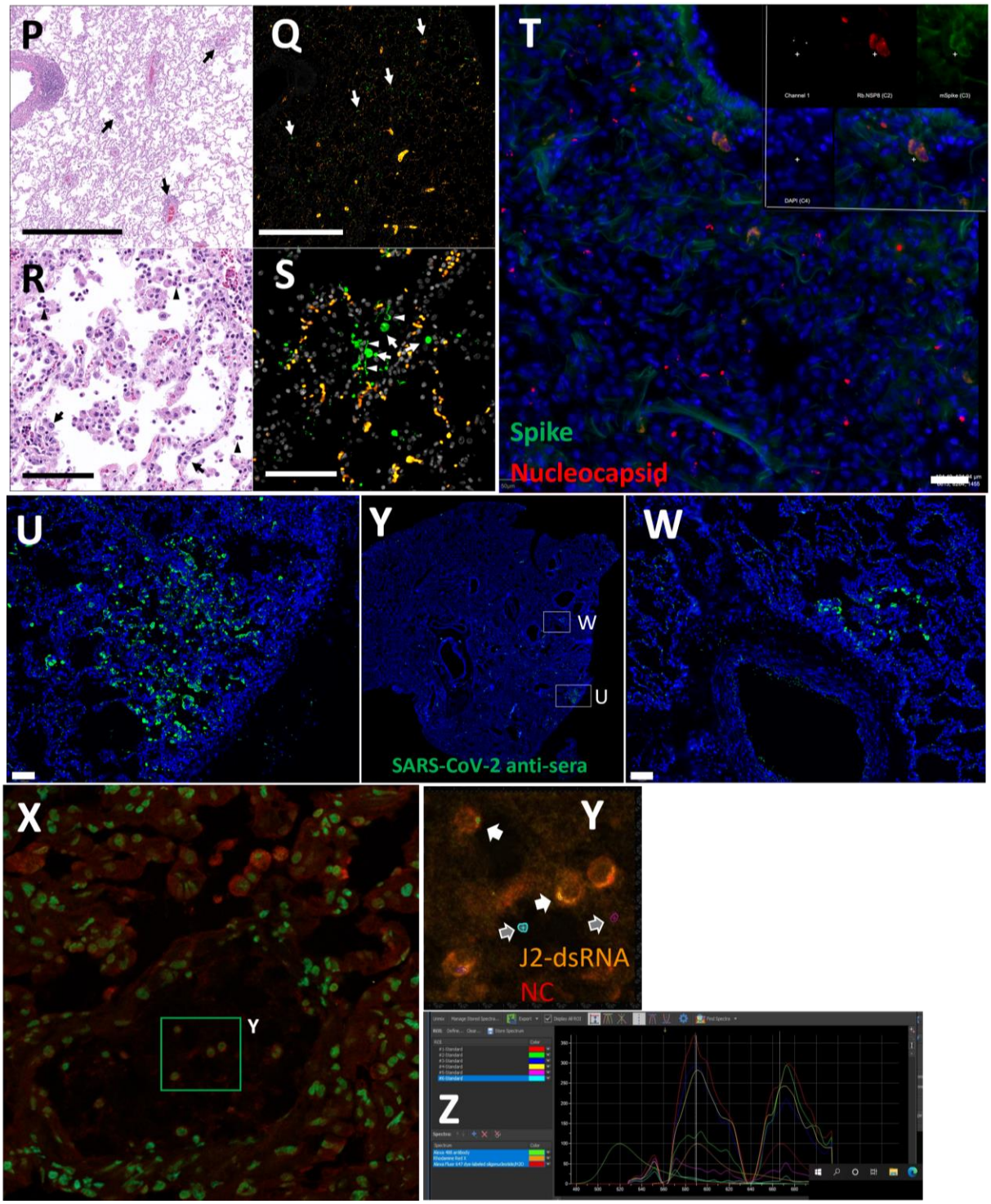

Figure 6. IN22 lung pathology and PET signal. (A-D) Lung PET volumes were isolated and overlaid on whole body CT scans. (A and B) Show lung volumes from 3-hour scan, side (A) and front (B) views shown. (C and D) Show lung volumes from 21-hour scan, side (C) and front (D) views shown. (E and F) Isolated lung PET volumes for each scan are shown independent of CT. (G) Sagittal z-slice from CT showing lungs. (H) PET signal overlaid on z-slice from G. (I)

1220 Transverse z-slice through torso from CT. (J) PET signal overlaid on z-slice from I. (K) Image of
1221 respiratory tract after necropsy. (L) Inset showing overt lung pathology in right lower lobe. (M)
1222 PET/CT signal from organ scan of respiratory tract. (N) PET/CT signal from M overlaid onto
1223 image from K. (O) PET/CT signal with CT contrast increased to observe pathology in lower right
1224 lung lobe. (P) H&E image of lung tissue showing areas of expanded alveolar space and
1225 inflammatory infiltrate (arrows). (Q) Immunofluorescence image of the same tissue from P.
1226 Green is SARS-CoV-2 anti-sera, red is background, and white is nuclear stain. White arrows
1227 indicate SARS-CoV-2 positive cells. (R) H&E image of lung tissue showing macrophages and
1228 neutrophils (arrowheads) and type II pneumocytes (arrows). (S) Immunofluorescence image
1229 showing infected cells of the alveoli (arrows) and lining the alveolar septa (arrowheads). Green
1230 is SARS-CoV-2 anti-sera, red is background, white is nuclear stain. All scale bars are 100 µM. (T)
1231 Fluorescent microscopy image of IN22 lung tissue. Spike shown in green, nucleocapsid shown in
1232 red, background in white, and Hoechst nuclear stain in blue. Scale bar 100 µM. (U, Y, W)
1233 Additional fluorescent microscopy images of lung tissue showing foci of infected cells. U and W
1234 are shown in low magnification Y. Green is SARS-CoV-2 anti-sera and blue is Hoechst nuclear
1235 stain. Scales bar 500 µM. (X-Z) Validation of dual antibody staining utilizing spectral imaging. (X)
1236 shows microscopy of J2 antibody with redX secondary and rabbit anti-NC monoclonal and Cy5
1237 secondary. (Y) Shows area within green square in X. White arrows point to regions of interest
1238 that are cell associated. Grey arrows indicate control regions of spectral evaluation. The areas
1239 evaluated by spectral imaging in (Y) are color coded and match with the spectra shown in (Z).

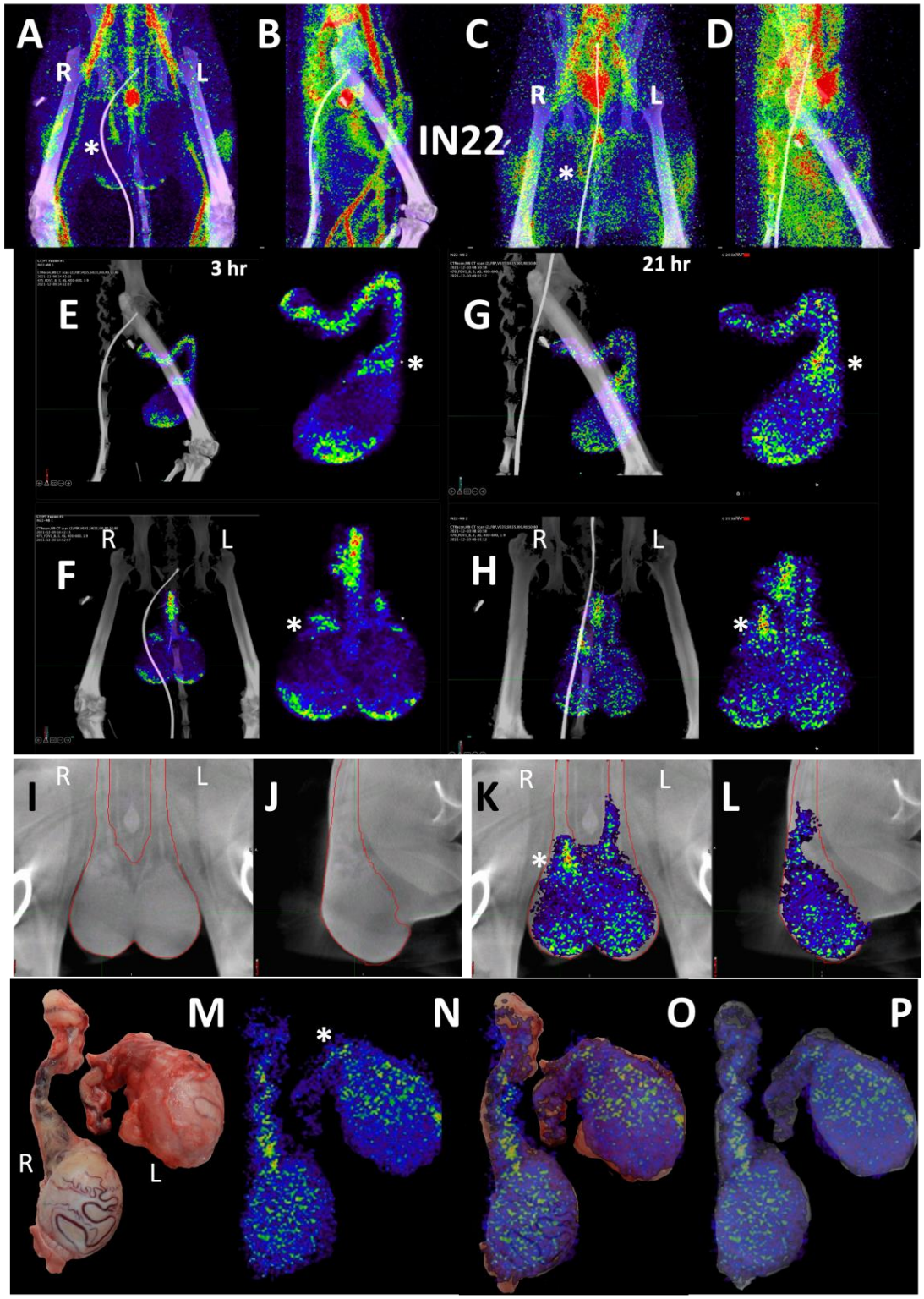

1240

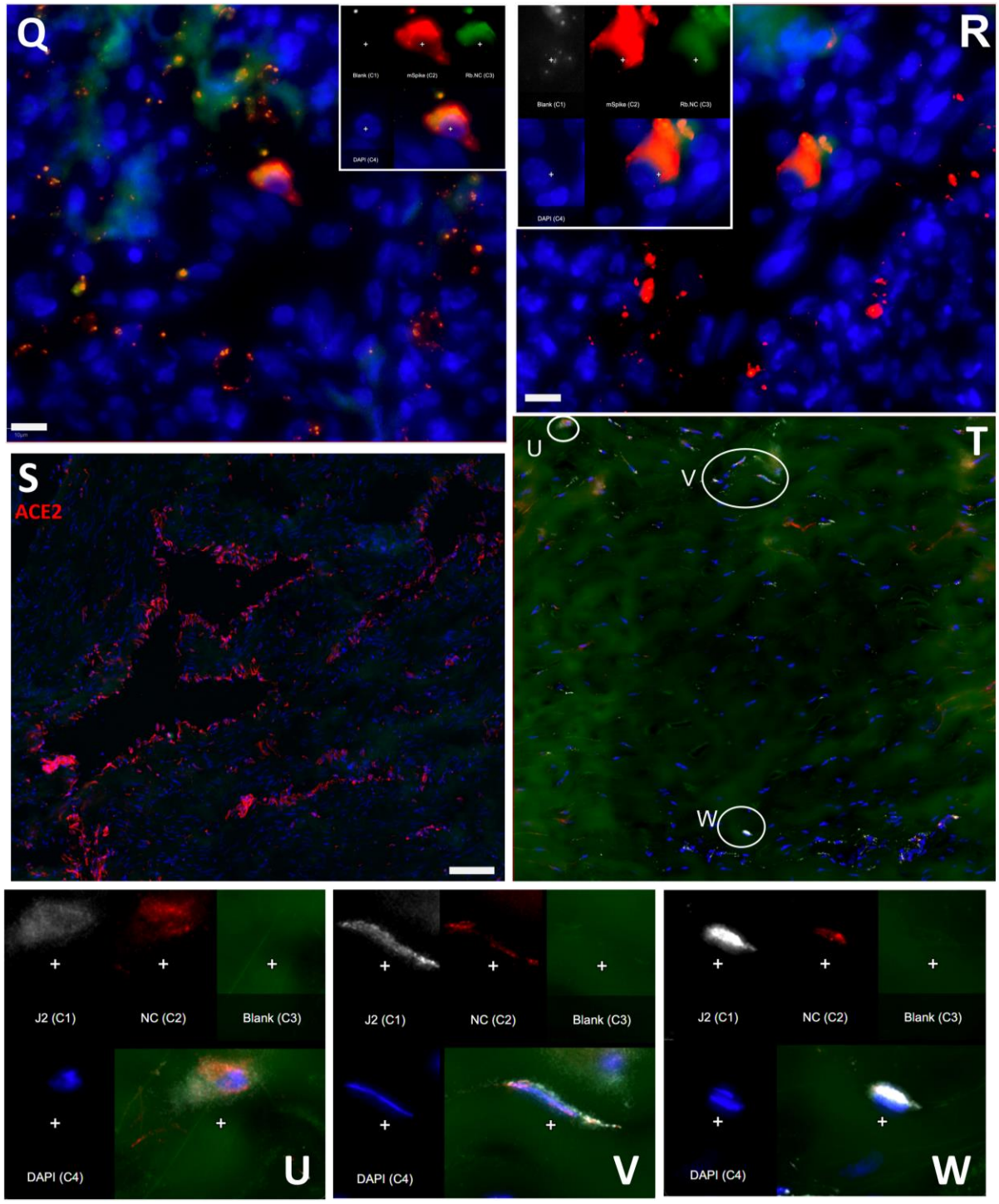

Figure 7. Male genital tract signal of IN22. (A and B) PET/CT images highlighting the lower abdomen of IN22 obtained 3-hours after probe administration. Front view (A) and side (B) both shown. (C and D) PET/CT images highlighting the lower abdomen of IN22 obtained 21-hours after probe administration. Front view (C) and side (D) both shown. (E and F) Isolated 3D volume of MGT from 3-hour scan overlaid with whole-body CT. Side (E) and front (F) views

shown. (G and H) Isolated 3D volume of MGT from 21-hour scan overlaid with whole-body CT. Side (G) and front (H) views shown. (I and J) Whole-body CT images of lower abdomen, red contours outline the testicles and spermatic cords. Front (I) and side (J) views shown. (K and L) 3D volume of MGT overlaid onto CT images from previous panels. (M) Image of testicles after necropsy. (N) PET signal from organ scan of testicles. (O) Overlay of PET signal onto image from panel M. (P) Overlay of PET signal onto CT signal from same scan. White asterisks mark location of pampiniform plexus in all previous panels. (Q and R) Fluorescence microscopy of SARS-CoV-2 infected cells in testicular tissue from IN22. Red is SARS-CoV-2 spike, green is SARS-CoV-2 nucleocapsid, white is background, and blue is Hoechst nuclear stain. Insets show channels independently, larger image is all channels merged. Scale bars 10 µM (S) Fluorescent microscopy image of corpus cavernosum tissue from an uninfected animal showing ACE2 staining in red, background in green, and Hoechst nuclear staining in blue. Scale bar 100 µM (T) Fluorescence microscopy of SARS-CoV-2 infected cells in penile tissue from IN22. White is dsRNA antibody J2, red is SARS-CoV-2 nucleocapsid, green is background, and blue is Hoechst nuclear stain. (U, V, and W) Show individual cells highlighted in T.

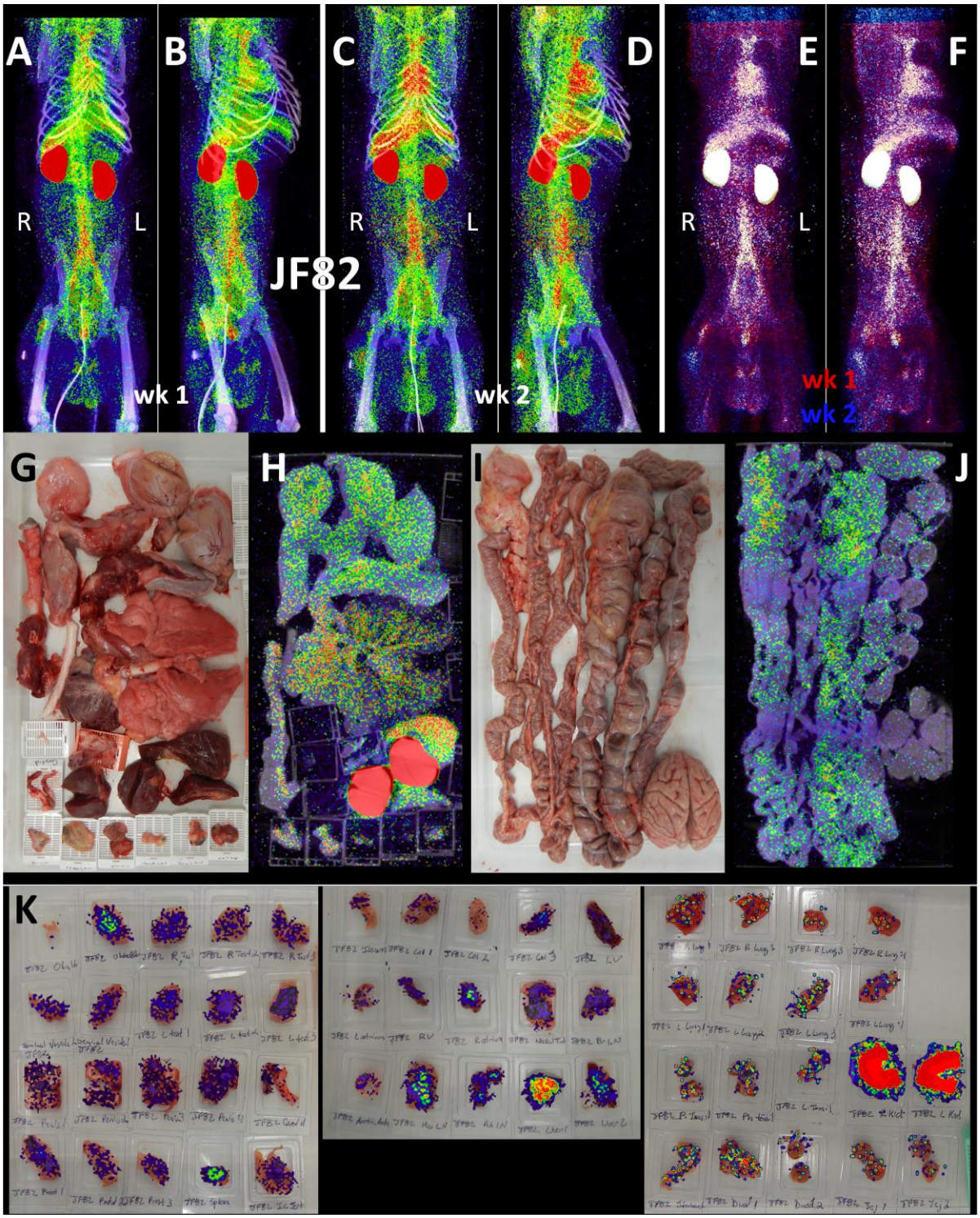

Figure 8. JF82 PET/CT images from week and week 2 necropsy scans. (A and B) Whole-body PET/CT scan of JF82 from 1-week post-infection. Front view (A) and side (B) both shown. (C and D) Whole-body PET/CT scans of JF82 2-weeks post infection. Front view (C) and side (D) both shown. Right and left labeled in front views (A and C). (E and F) Overlay of the week 1 scan

(shown in red) and the week 2 scan (shown in blue). Front (E) and side (F) views both shown. (G) Organ tray post necropsy and (H) PET/CT image. (I) Second organ tray post necropsy and (J) PET/CT image. (K) Overlay of PET signal onto photograph of tissue cassettes.

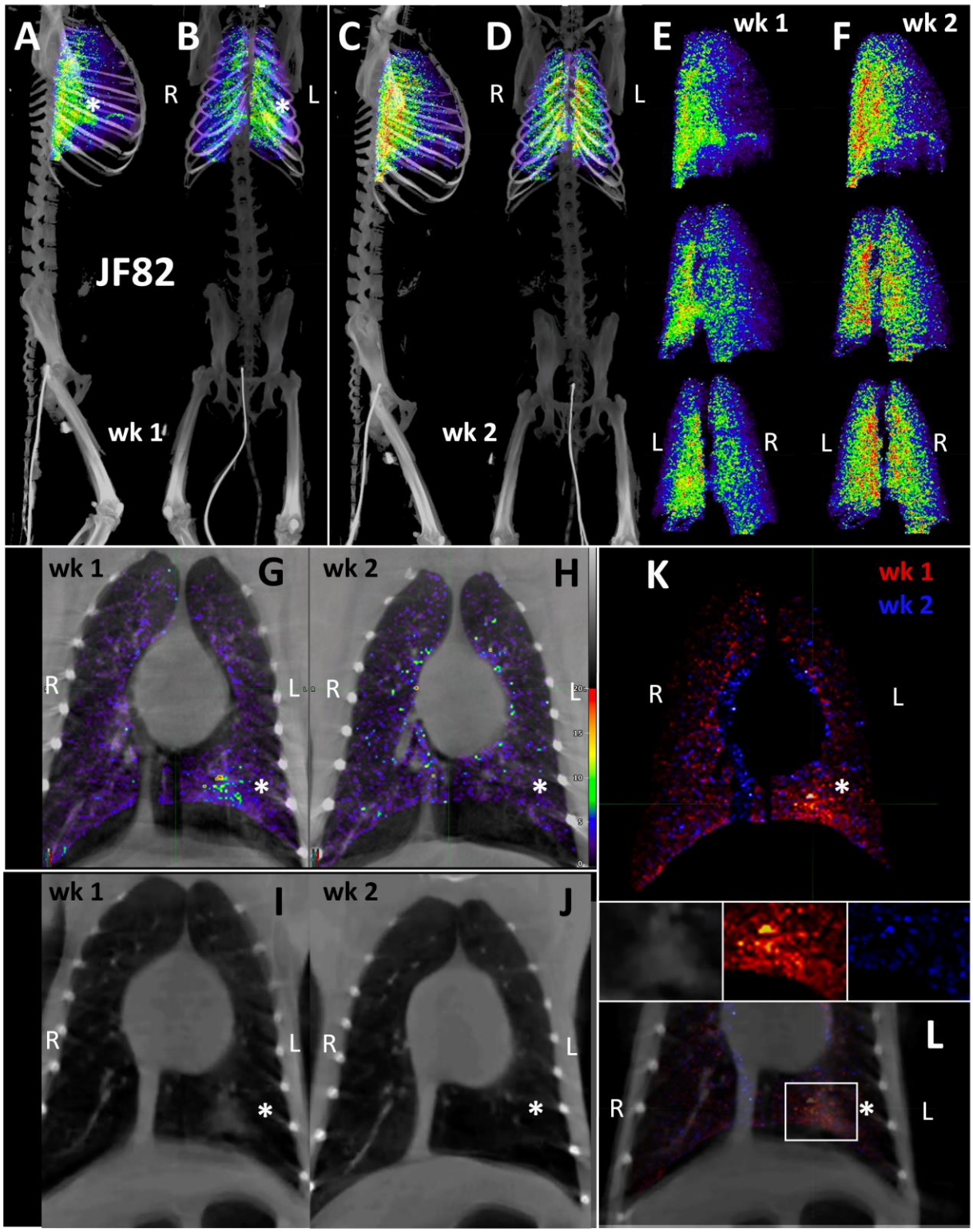

Figure 9. JF82 lung pathology and PET signal from two timepoints. (A-D) Lung PET volumes were isolated and overlaid on whole body CT scans. (A and B) Show lung volumes from 1-wee

scan, side (A) and front (B) views shown. White asterisk indicates location of lung pathology highlighted below. (C and D) Show lung volumes from 2-week scan, side (C) and front (D) views shown. (E and F) Isolated lung PET volumes for each scan are shown independent of CT. (G and H) Overlay of single z-image of PET signal onto single z-image of CT in the lungs at week 1 (G) and week 2 (H). (I and J) Single z-image of CT used in G and H shown independent of PET signal for week 1 (I) and week 2 (J). (K) Overlay of week 1 (shown in red) and week 2 (shown in blue) PET signal. (L) Overlay from K shown with CT image to localize PET signal. Insets above show, CT, week 1, and week 2 signal from left to right. White asterisk indicates location of left lung pathology in all panels.

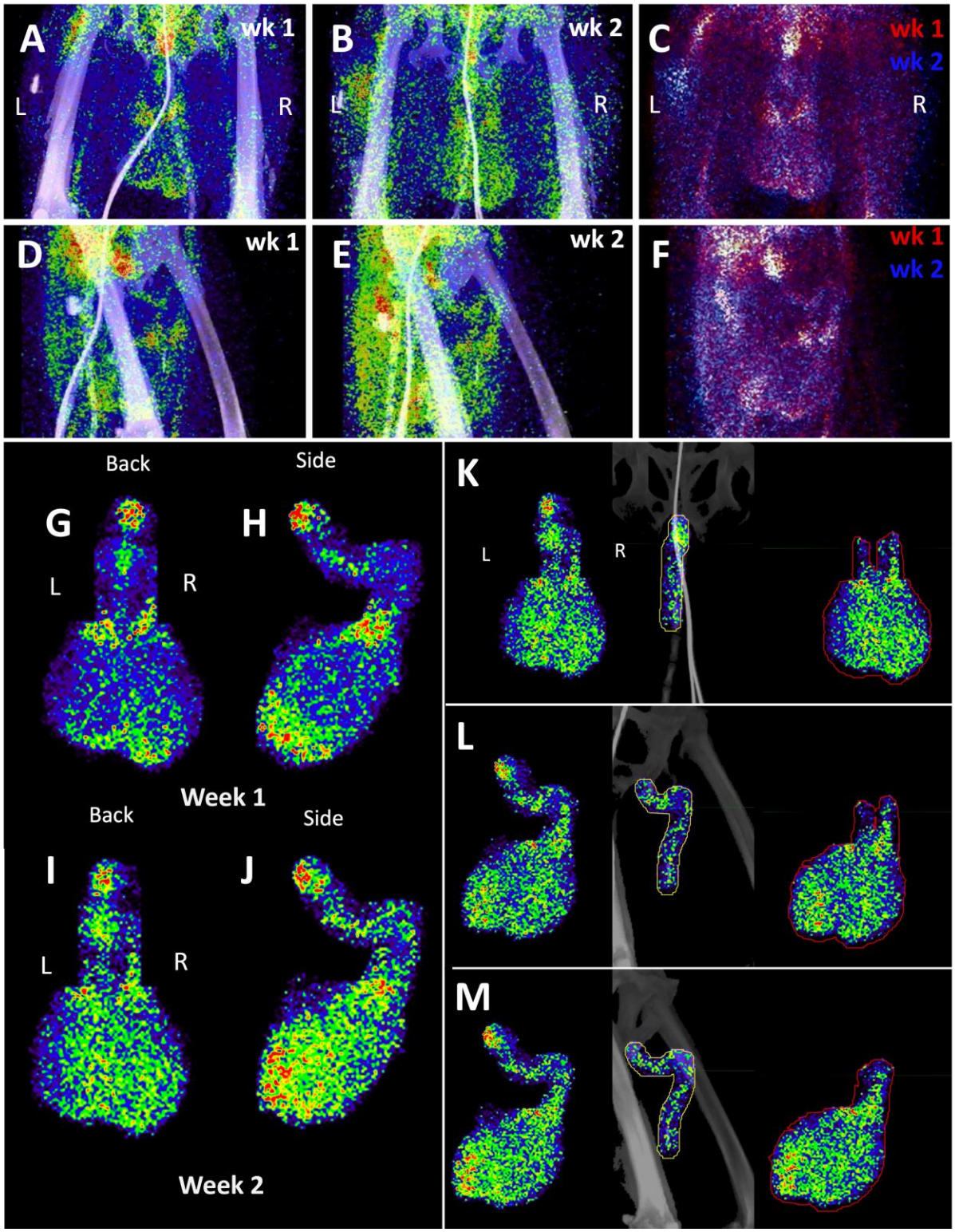
A
wk 1
L
R
B
wk 2
L
R
C
wk 1
wk 2
L
R
D
wk 1
E
wk 2
F
wk 1
wk 2
Back
Side
G
H
L
R
Week 1
Back
Side
I
J
L
R
Week 2
K
L
R
L
M

1353

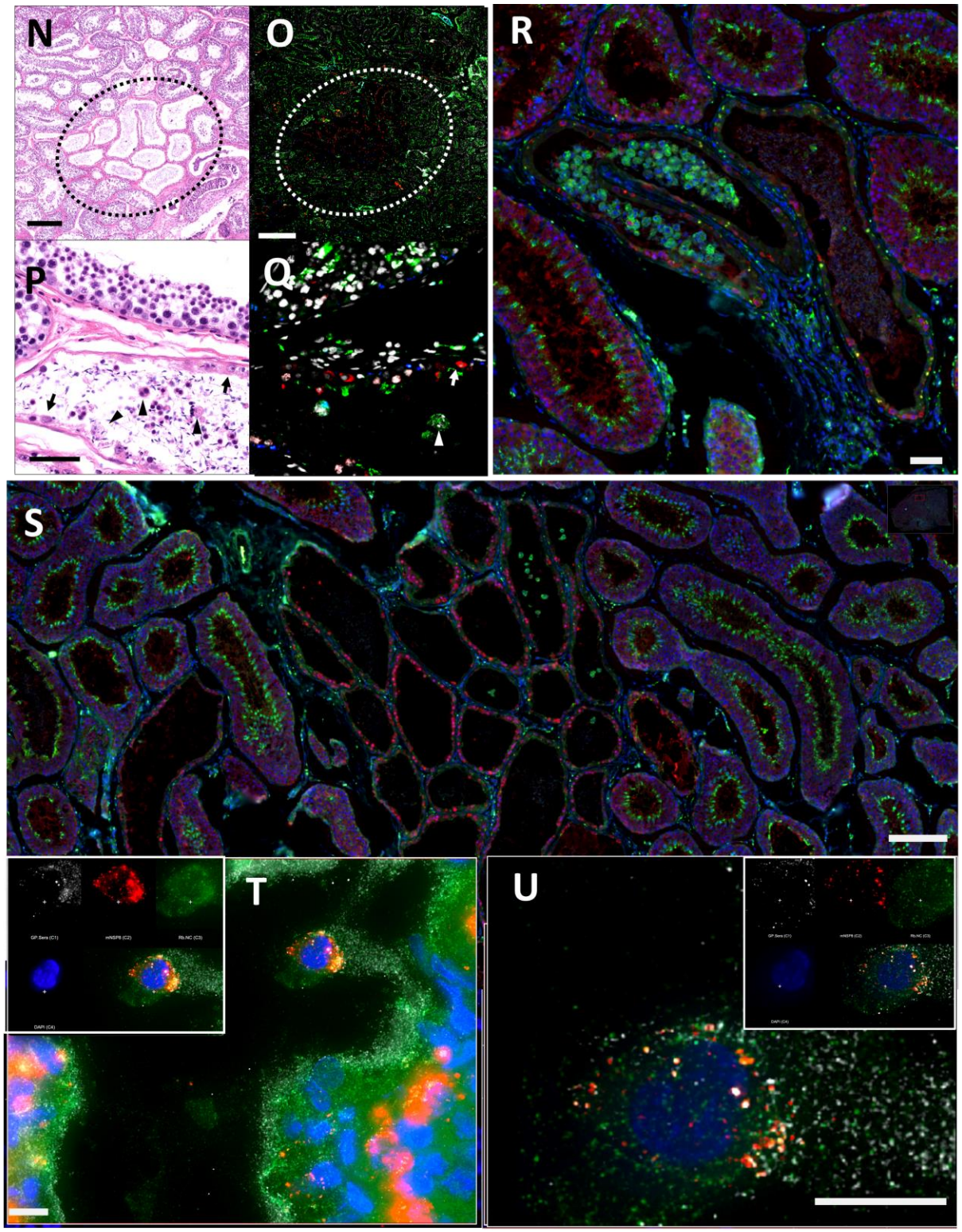

Figure 10. Male genital tract signal in JF82. (A and B) Front view PET/CT images highlighting the lower abdomen of JF82 at 1-week (A) and 2-weeks (B). (C) Overlay of week 1 (shown in red) and week 2 (shown in blue) PET signal. (D and E) Side view of same images shown in A and B. (F)

side view of overlay shown in C. (G and H) Isolated MGT volume from week 1 scan. Back (G) and side (H) views shown. (I and J) Isolated MGT volume from week 2 scan. Back (I) and side (J) views shown. (K, L, and M) Isolated MGT volume from week 2 with isolated penile and testicular signal. Back (K), rotated 45° (L), and side (M) views shown. (N) H&E stain of JF82 testicular tissue. Degenerate seminiferous tubules highlighted in black oval. Scale bar 500 µM. (O) Fluorescent microscopy shows a similar area of degenerate tubules. Green is CD206, red caspase 3, and white nuclear stain. Scale bar 500 µM. (P) Higher magnification image of degenerate tubules. Intraluminal macrophages (arrowheads) and Sertoli cells (arrows) are shown inside tubules. Scale bar 50 µM (Q) Higher magnification of image in O shows Sertoli cells (arrow) staining with caspase 3 and macrophages (arrowhead) staining with CD206. Scale bar 50 µM. (R) Fluorescent microscopy image showing degenerate tubule full of intraluminal macrophages. Red is caspase 3, green is CD206, and blue is nuclear stain. Scale bar 50 µM. (S) Lower magnification microscopy image of degenerate and healthy tubules. Red is caspase 3, green is CD206, and blue is nuclear stain. Scale bar 200 µM. (T and U) Fluorescent microscopy images of infected cells in testicular tissue of JF82. White is SARS-CoV-2 anti-sera, red is NSP8, green is nucleocapsid, and blue is Hoechst nuclear stain. Insets show individual channels, larger image is merge. Scale bars 10 µM.

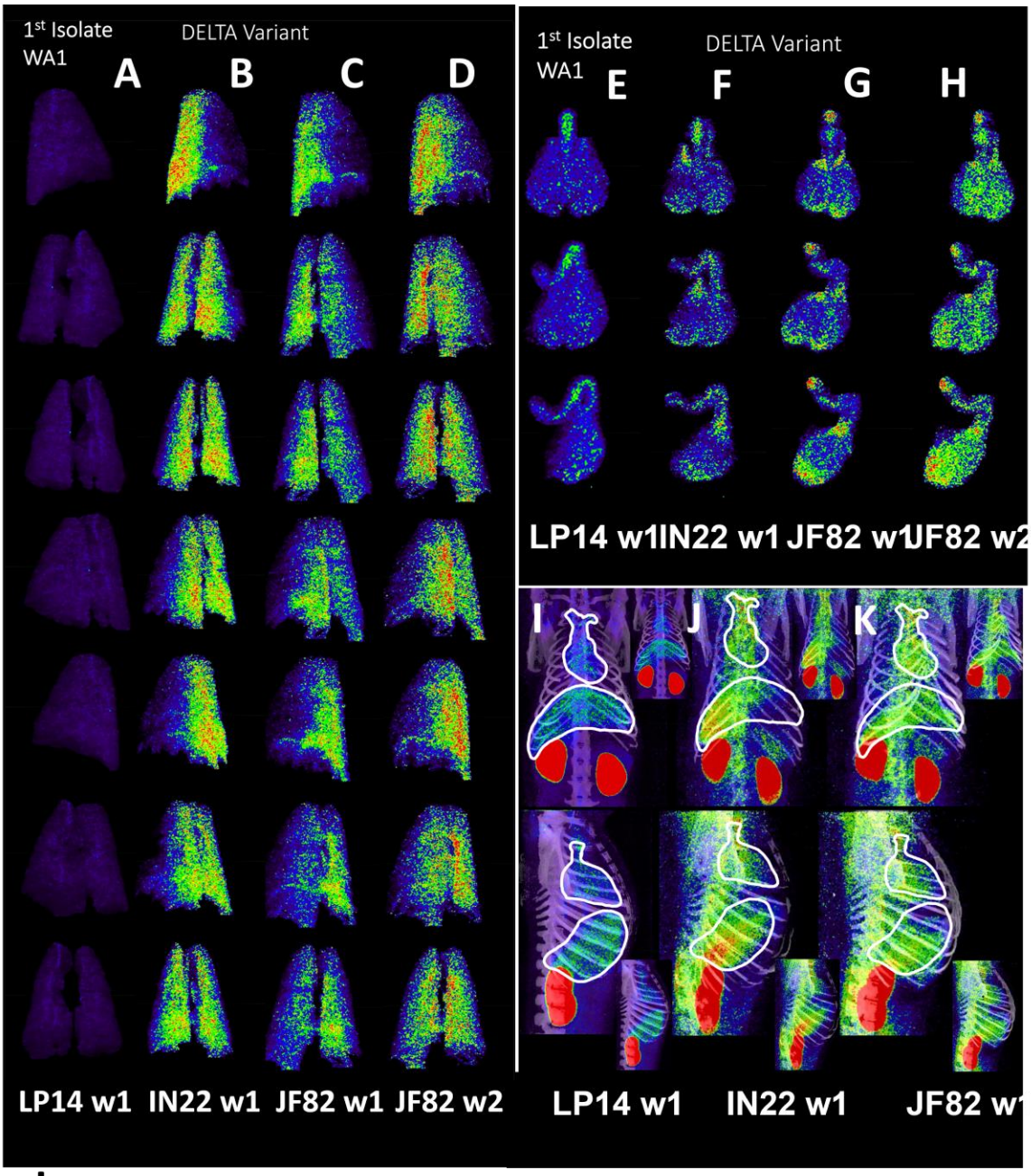
1st Isolate
WA1
DELTA Variant
A
B
C
D
LP14 w1
IN22 w1
JF82 w1
JF82 w2
1st Isolate
WA1
DELTA Variant
E
F
G
H
LP14 w1
IN22 w1
JF82 w1
JF82 w2
I
J
K
LP14 w1
IN22 w1
JF82 w1

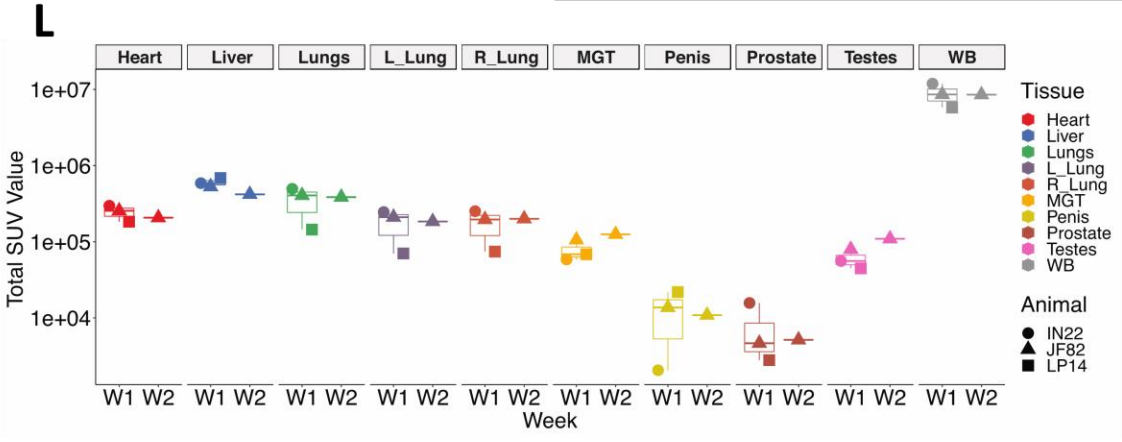
L
Heart
Liver
Lungs
L_Lung
R_Lung
MGT
Penis
Prostate
Testes
WB
Total SUV Value
1e+07
1e+06
1e+05
1e+04
W1 W2
Week
Tissue
Heart
Liver
Lungs
L_Lung
R_Lung
MGT
Penis
Prostate
Testes
WB
Animal
IN22
JF82
LP14

1403

Figure 11. Comparison of SUVs across animals and timepoints. (A-D) Complete rotation series of lung PET volumes for LP14 (A), IN22 (B), JF82 week 1 (C), and JF82 week 2 (D). (E-H) Front, rotated 45°, and side views of MGT PET volumes for LP14 (E), IN22 (F), JF82 week 1 (G), and JF82 week 2 (H). (I-K) Front and side views of whole-body scans, white lines indicate volumes taken for heart and lungs for LP14 (I), IN22 (J), and JF82 week 1 (K). Insets show each image without white outlines. (L) Total SUVs for whole-body scans and each individual volume isolated displayed in graph. Animals are indicated by icon shape and volumes by color.

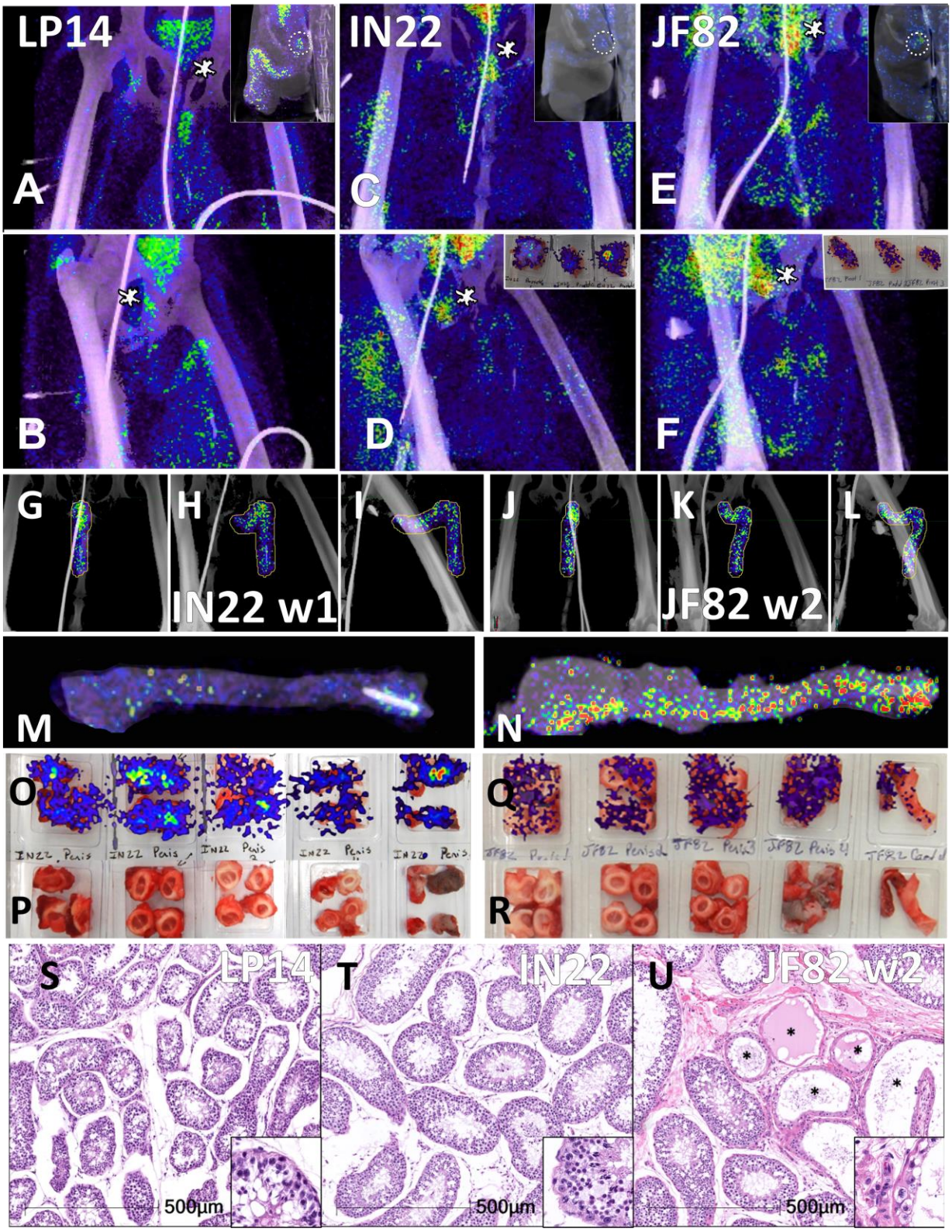

Figure 12. Comparison of prostate and penile signal between animals. (A-F) PET/CT signal in lower abdomen for each animal at 1-week post-infection. LP14 front (A) and rotated 45° (B),

1417 IN22 front (C) and rotated 45° (D), JF82 front (E) and rotated 45° (F). Asterisks mark location of
1418 prostate. Insets show sagittal z-slice of each animal highlighting prostate signal (white circle).
1419 (G-I) PET/CT volume of penis for IN22. Front (G), rotated 45° (H), and side (I) views shown. (J-L)
1420 PET/CT volume of penis for JF82 at 2-weeks post-infection. Front (J), rotated 45° (K), and side (L)
1421 views shown. (M) PET/CT signal of IN22 penis after necropsy. (N) PET/CT signal of JF82 penis
1422 after necropsy. (O) PET/CT signal overlaid onto an image of tissue cassettes (P) containing
1423 penile tissue of IN22. (Q) PET/CT signal overlaid onto an image of tissue cassettes (R) containing
1424 penile tissue of JF82. (S-U) H&E images of testicular tissue from each animal. LP14 (S) and IN22
1425 (T) shows normal spermatogenesis and tissue architecture. IN22 (U) shows degenerate tubules
1426 (asterisks) interspersed among healthy tubules. Scale bars all 500 µM.
1427

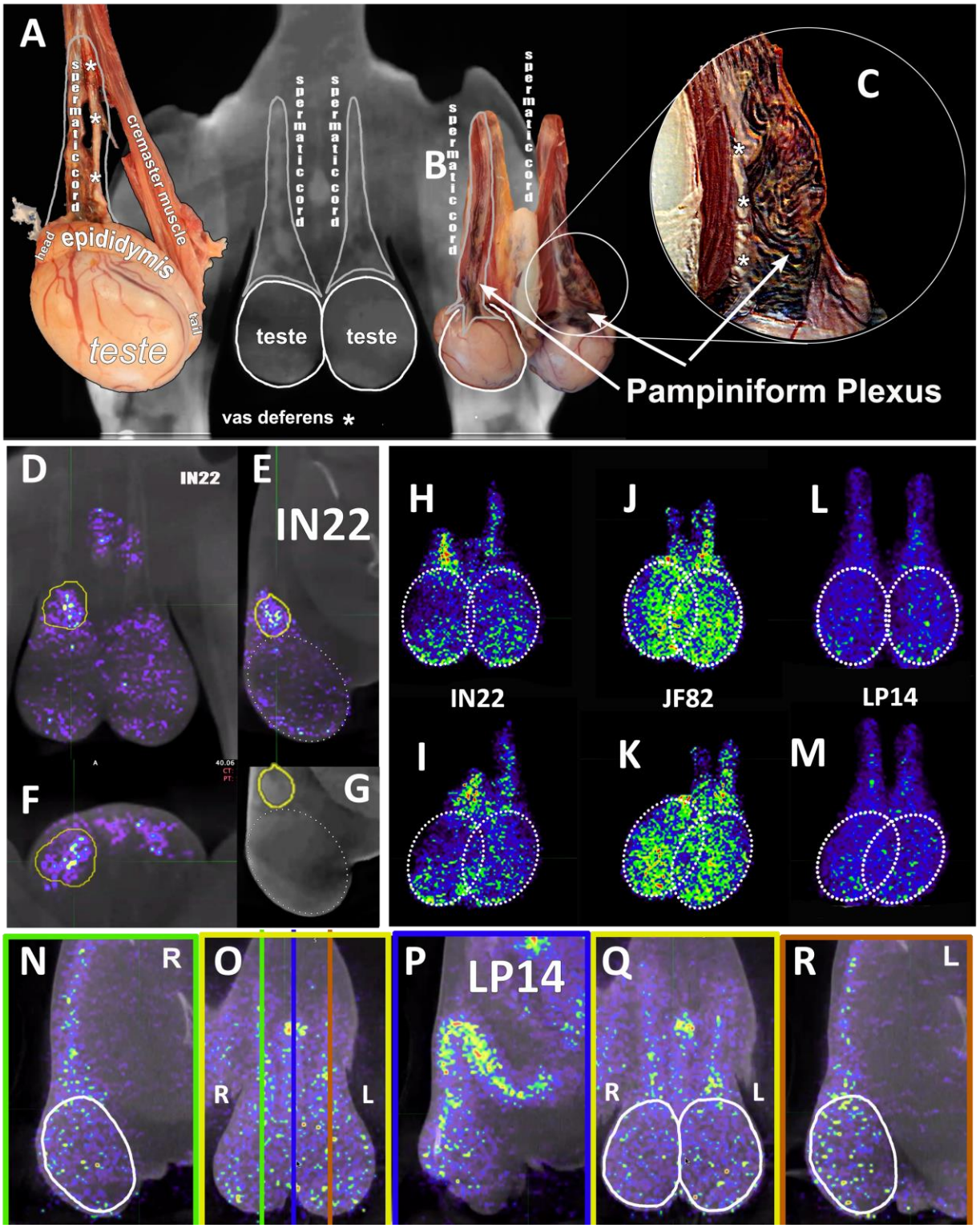

Figure 13. PET signal associated with the pampiniform plexus. (A) Labeled dissection showing anatomical structure of a macaque testis. (B) CT image of testes and associated image showing the matching anatomical features of the spermatic cord. (C) Inset highlighting the location and

appearance of the pampiniform plexus. White asterisks mark the vas deferens in all images. (D-F) Single z PET/CT images of IN22 highlighting the PET signal associated with the pampiniform plexus (yellow volume) from the frontal (D), sagittal (E), and transverse (F) plane. (G) CT image used in E to highlight signal associated with pampiniform plexus (yellow volume). (H-L) Isolated 3D volumes of MGT PET signal shown from the front for IN22 (H), JF82 (J), and LP14 (L). White circles outline testes. (I, K, M) Volumes from H, J, and L rotated 45°. (N) Sagittal z-slice of PET/CT of LP14 showing right testis. (O) Frontal z-slice of PET/CT, colored lines correspond to sagittal slices shown in N, P, and R. (P) Sagittal z-slice of PET/CT showing penile tissue. (Q) Frontal z-slice highlighting the testicular tissue in white ovals. (R) Sagittal z-slice of PET/CT showing left testis of LP14. White ovals highlight signal associated with testes and not pampiniform plexus.

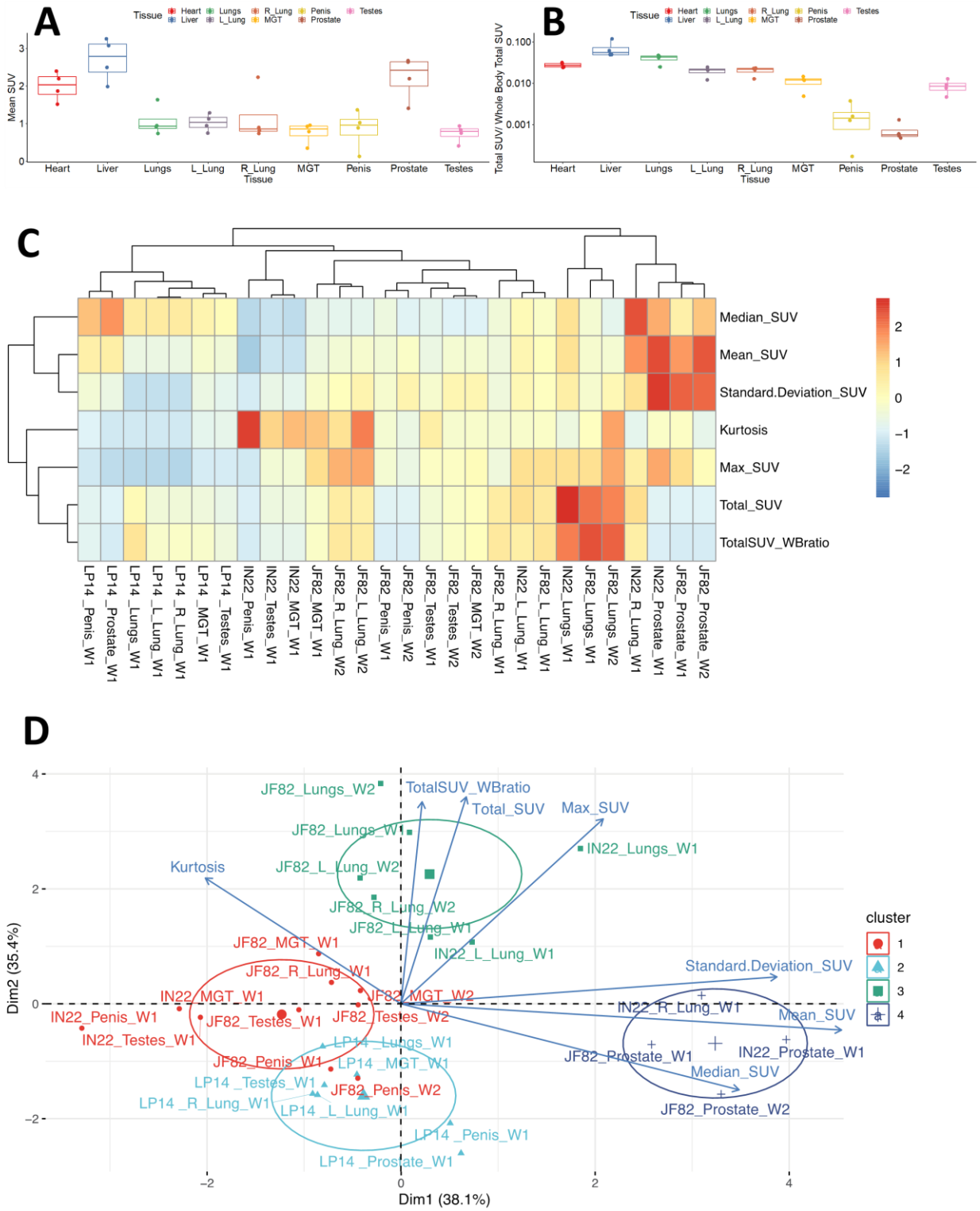

Figure 14. Principle components analysis of SUV measures. (A) Mean SUV values from isolated tissue volumes. (B) The ratio of total SUV for each tissue volume to whole-body total SUV. (C) Heat map showing clustering of tissues and parameters measured from the PET data. (D)

1449 Principal components analysis of measures showing hierarchical clustering of tissues and
1450 measures.
1451